Regional Simulation of Indian summer Monsoon Intraseasonal Oscillations at Gray Zone Resolution

Xingchao Chen[1, 2, 3], Olivier M. Pauluis[1, 2], Fuqing Zhang[3]

[1]Center for Prototype Climate Modeling, New York University in Abu Dhabi, Abu Dhabi, United Arab Emirates
[2]Courant Institute of Mathematical Sciences, New York University, New York, New York, USA
[3]Department of Meteorology and Atmospheric Science, and Center for Advanced Data Assimilation and Predictability Techniques, The Pennsylvania State University, University Park, Pennsylvania, USA

Correspondence to:

Dr. Xingchao Chen
Email: xzc55@psu.edu

Abstract

Simulations of the Indian summer monsoon by cloud-permitting WRF model at gray zone resolution are described in this study, with a particular emphasis on the model ability to capture the Monsoon Intraseasonal Oscillations (MISO). Five boreal summers are simulated from 2007 to 2011 using the ERA-Interim reanalysis as lateral boundary forcing data. Our experimental set-up relies on a high horizontal resolution of 9km to capture deep convection without the use of a cumulus parameterization. When compared to simulations with coarser grid spacing (27-km) and using the cumulus scheme, our approach results in a reduction of the biases in mean precipitation and in more realistic reproduction of the low frequency variability associated with MISO. Results show that the model at gray zone resolution captures the fundamental features of the summer monsoon. The spatial distributions and temporal evolutions of monsoon rainfall in WRF simulations are verified qualitatively well against observations from the Tropical Rainfall Measurement Mission (TRMM), with regional maxima located over West Ghats, central India, Himalaya foothills and the west coast of Myanmar. The onset, breaks and withdrawal of the summer monsoon in each year are also realistically captured by the model. MISO phase composites of monsoon rainfall, low-level wind and precipitable water anomalies in the simulations are compared qualitatively with the observations. Both the simulations and observations show a northeastward propagation of the MISO, with the intensification and weakening of Somali Jet over the Arabian Sea during the active and break phases of the Indian summer monsoon.

1. Introduction

The Indian summer monsoon (ISM) is the most vigorous weather phenomena affecting the Indian subcontinent every year from June through September (JJAS). It contributes about 80% of the total annual precipitation over the region (Jain and Kumar, 2012; Bollasina, 2014) and has substantial influences to the agricultural and industrial productions in India. The ISM exhibits strong low frequency variability in the form of "active" and "break" spells of monsoon rainfall (Goswami and Ajayamohan, 2001), with two dominant modes on timescales of 30-60 days (Yasunari, 1981; Sikka and Gadgil, 1980) and 10-20 days (Krishnamurti and Bhalme, 1976; Chatterjee and Goswami, 2004). The low-frequency mode is generally known as the Monsoon Intraseasonal Oscillation (MISO), which is closely related to the Boreal Summer Intraseasonal Oscillations (BSISO, Krishnamurthy and Shukla, 2007; Suhas et al., 2013; Sabeerali et al., 2017; Kikuchi et al., 2012; Lee et al., 2013) and characterized by a northeastward propagation of the precipitation from the Indian Ocean to the Himalayan foothills (Jiang et al., 2004). The MISO not only affects the seasonal mean strength of the ISM, but also plays a fundamental role in the interannual variability and predictability of the ISM (Goswami and Ajayamohan, 2001; Ajayamohan and Goswami, 2003). The MISO phases occurring at the early and late stages of the ISM also has considerable influences on the onset and withdrawal of the ISM, which, in another word, determining the length of the rainy season (Sabeerali et al., 2012). Hence, a more accurate forecast of the MISO assumes significance. The MISO is influenced by a number of physical processes (Goswami, 1994). Its interactions with the mean monsoon circulation and other tropical oscillations make its propagating characteristics very complex (Krishnamurthy and Shukla, 2007).

General circulation models (GCMs) are broadly used to simulate the large-scale circulation and seasonal rainfall climatology of the ISM. Results show that GCMs are able to capture the fundamental features of the monsoon circulation reasonably well. However, the monsoon precipitation is still a rigorous test for most GCMs (e.g., Bhaskaran et al., 1995; Lau and Ploshay, 2009; Chen et al., 2011). Also, the skill of the current generations of GCMs in simulating and predicting the MISO remains poor (Ajayamohan et al., 2014; Lau and Waliser, 2011). The computer power available nowadays constrains most GCMs to perform long-term global simulations with a horizontal spacing lager than 100 km (Lucas-Picher et al., 2011, though a few GCMs can go down to 25 km for tropical cyclones forecast, like GFDL HiRAM). As a result, the GCMs cannot well capture the high frequency atmospheric variance and regional dynamics associated with the MSIO, which also leads to a systematic bias in simulating the ISM rainfall (Goswami and Goswami, 2016; Srinivas et al., 2013). Increasing the spatial resolution therefore is the way for GCMs (of course not the only way) to improve the MISO simulation and to reduce the systematic model biases (e.g., Ramu et al., 2016; Rajendran and Kitoh, 2008; Oouchi et al., 2009). However, the high resolution global simulations usually require significant computational resources that most climate modeling groups cannot afford.

An alternative approach to improve the ISM and MISO simulations is the use of regional climate models (RCMs). RCMs dynamically downscale the GCM simulations or reanalysis and perform a climate simulation over a certain region of the globe (Prein et al., 2015; Giorgi, 2006). Using same computer resources, RCMs are able to perform the climate simulation with much higher spatial resolution and are expected to better capture the high pass atmospheric variance and resolve the important regional forcings associated with topography, land-sea contrast and land cover (Bhaskaran et al., 1996; Dash et al., 2006). Many previous studies found that better

ISM and MISO simulations can be achieved in the high resolution (typically 50km or less) RCMs than that in the GCMs with coarser grid spacing (e.g., Bhaskaran et al., 1998; Kolusu et al., 2014; Lucas-Picher et al., 2011; Srinivas et al., 2013; Raju et al., 2015; Samala et al., 2013; Vernekar and Ji, 1999; Mukhopadhyay et al., 2010; Saeed et al., 2012). Nonetheless, apparent biases of the MISO simulations can still be found in the most previous RCM studies. One principle reason is, to reduce the computational requirements, the spatial resolutions used in the previous RCM studies are still not high enough to resolve the convection explicitly, and convective activity is represented by the cumulus parameterization schemes in the simulations. However, the organization of convection is the primary mechanism for simulating the realistic MISO (Ajayamohan et al., 2014). Hence, using cumulus schemes may introduce a systematic bias in simulating the MISO and the monsoon rainfall climatology (Mukhopadhyay et al., 2010; Das et al., 2001; Ratnam and Kumar, 2005). In addition, the cumulus parameterization schemes can also interact with other parameterization schemes, such as the planetary boundary layer, radiation and microphysical schemes, which may imply far-reaching consequences through nonlinearities and affects the simulation of the MISO (Prein et al., 2015).

The alternative to the use of a convective parameterization is to rely on the internal dynamics to resolve convective motion. A consensus view is that Cloud Resolving Models (CRMs) must have a horizontal resolution of at least 2km to resolve the dynamics of deep convection, albeit even finer resolution are necessary in order to adequately resolve the turbulent motions in convective systems (Bryan et al., 2003). However, Pauluis and Garner (2006) have shown that cloud-permitting model with horizontal resolution as coarse as 12km can accurately reproduce the statistical behavior of convection simulated at much finer resolution. This implies that a

coarse resolution CRM, one in which convective motion is under resolved, can nevertheless capture adequately the impacts of convective motions on large scale atmospheric flows.

Recently, Wang et al. (2015, W15 hereafter) simulated two MJO events observed during the CINDY/DYNAMO campaign using a convection-permitting regional model with 9-km grid spacing. The authors compared the simulations with multiple observational datasets and found that the RCM at this resolution can successfully capture the intraseasonal oscillations over the tropical oceans. The horizontal grid spacing of 9 km used in W15 is not adequate for individual convective cells, but enough to resolve the organized mesoscale convective systems and their upscale impacts and coupling with large-scale dynamics. Hence, they called the 9-km grid spacing as gray zone resolution in regional convection-permitting climate simulation. The convection-permitting RCMs at the gray zone resolution have the twin advantages of (1) using much less computational resources than that required by the typical cloud-resolving simulations (usually, grid spacing should be smaller than 2 km) and (2) avoid using the cumulus parameterization schemes. The primary objective of the present study is to evaluate the ISM and MISO simulations in the RCM at the gray zone resolution, which could be an affordable and efficient way for most climate model groups to achieve a cloud-permitting MISO simulation. The paper is constructed as follows. Section 2 provides a brief description of the model and the data used. Section 3 presents the model simulated mean ISM features and seasonal evolutions of the rainfall over the monsoon region. The simulated MISO are described and compared with the observations and reanalysis in section 4. Section 5 gives the concluding remarks of the study.

2. Experimental setup and observational datasets

The model configuration here is similar with the one used in W15. The Advance Research WRF model (Skamarock et al., 2008), version 3.4.1, is used to simulate the ISMs over the Indian subcontinent from 2007 to 2011. Simulations are performed over a single domain that covers the most of South Asia with 777×444 grid points and 9-km grid spacing (Fig. 1). There are 45 vertical levels with a nominal top at 20 hPa and 9 levels in the lowest 1 km. Vertically propagating gravity waves have been suppressed in the top 5 km of the model with the implicit damping scheme (Klemp et al., 2008). The high model top (~ 27 km) allows the development of deep convection, especially over the mountainous area. While the sponge layer above the tropopause can damp the gravity waves produced by the deep convective activity or steep terrain and prevent the upward propagating gravity-wave energy be bounced back to the troposphere. The simulation employs the unified Noah land surface physical scheme (Chen and Dudhia, 2001), the GCM version of the Rapid Radiative Transfer Model (RRTMG) longwave radiation scheme (Iacono et al., 2008), the updated Goddard shortwave scheme (Shi et al., 2010) and the WRF Double-Moment (WDM) microphysics scheme (Lim and Hong, 2010) from WRF V3.5.1 with an update on the limit of the shape parameters and terminal speed of snow. In W15, the authors used the Yonsei University (YSU) boundary layer scheme (Hong et al., 2006) to simulate the subgrid-scale meteorological processes within the planetary boundary layer. However, we find that there exists an apparent dry bias in simulating the ISM precipitation after a long-term integration when YSU boundary layer scheme is used. In order to improve the simulation, boundary layer scheme used for this study has been changed to the new version of the asymmetric convective model (ACM2, Pleim, 2007). Hu et al. (2010) evaluated the different boundary schemes used in the WRF model and found that ACM2 scheme can better simulate the

166 boundary meteorological conditions of the Texas region during summer than YSU scheme.
167 Nevertheless, the sensitivity of ISM simulations to the boundary-layer schemes is still deserve
168 closer analysis and quantifications in the future, which is out of the scope of the present study.
169 Our model configuration does not use any parameterization for deep convection, but rather relies
170 on the internal dynamics to capture the impact of convective activity.

171 Five boreal summers are simulated from 2007 to 2011 in this study. The 6-hourly
172 ERA-Interim reanalysis (Dee et al., 2011) is used as the initial and boundary conditions for the
173 simulations, and sea surface temperature (SST) is updated every 6 hours using the ERA-Interim
174 SST data. The ERA-Interim reanalysis is produced with a sequential data assimilation scheme,
175 advancing forward in time using 12-hourly analysis cycles. The zonal and meridional winds in
176 the reanalysis are directly assimilated from observational data, thus the large scale monsoon
177 circulation is well captured in the reanalysis. The Indian summer monsoon precipitation
178 climatology in ERA-Interim has also been compared with that in other reanalysis datasets, and
179 the results show that ERA-Interim has the highest skill to reproduce the Indian summer monsoon
180 rainfall though obvious biases can still be found (Kishore et al., 2016; Lin et al., 2014). The
181 model integrations start from 0000 UTC 20 April in each year. For the first 3 days, a spectral
182 nudging is applied to relax the horizontal wind with a meridional wave number 0-2 and a zonal
183 wavenumber 0-4, which constrains the large-scale flow and convergence in the domain and
184 allows the mesoscale to saturate in the spectral space (W15). The simulations are integrated until
185 October 30 for each year in order to capture the withdrawal of the ISM in different years. The
186 simulated spatial distributions and temporal variations of surface rainfall are verified against the
187 3-hourly 0.25^{o} TRMM 3B42 rainfall product version 7A, while the large-scale circulations and
188 atmospheric conditions in the simulations are verified against the ERA-interim reanalysis.

189 Besides the control simulations at 9 km resolution (WRF-gray hereafter), another set of
190 numerical simulations with coarser grid spacing (27km, WRF-27km hereafter) are also
191 conducted in this study to evaluate the extent to which the cloud-permitting simulations at gray
192 zone resolution can improve the simulation of the ISM and MISO. The configuration of the
193 coarse simulations is similar with WRF-gray except cumulus parameterization scheme is used to
194 represent the subgrid-scale convective activity. Mukhopadhyay et al. (2010) investigated the
195 impacts of different cumulus schemes on the systematic biases of ISM rainfall simulation in the
196 WRF RCM. They compared the simulations conducted with three different convective schemes,
197 namely the Grell–Devenyi (GD, Grell and Dévényi, 2002), the Betts–Miller–Janjić (BMJ, Janjić,
198 1994; Betts and Miller, 1986), and the Kain–Fritsch (KF, Kain, 2004) schemes. Results show
199 that KF has a high moist bias while GD shows a high dry bias in simulating the monsoonal
200 rainfall climatology. Among these three schemes, BMJ can produce the most reasonable
201 monsoonal precipitation over the Indian subcontinent with the least bias. Similar results can also
202 be found in Srinivas et al.(2013). Hence, the BMJ scheme has been used in the WRF-27km
203 simulations.

204 Fig. 2 shows the daily surface precipitation averaged over the Indian subcontinent (shown by
205 the blue polygon in Fig. 1) from TRMM observation, WRF-gray and WRF-27km during the
206 monsoon seasons (JJAS). An apparent moist bias of surface precipitation can be found for all 5
207 years (2007 to 2011) in WRF-27km, while this systematic bias is reduced considerably in
208 WRF-gray. One reason of the moist bias reduction is the topography is better resolved in
209 WRF-gray than that in WRF-27km (the spatial resolution of topography is 3-times higher in
210 WRF-gray). Thus, the local convective activity is better simulated and the total surface
211 precipitation is less over the Himalaya foothills and West Ghats in WRF-gray (not shown here).

Besides the mountainous area, surface rainfall simulation over the plain and oceanic regions also shows high moist bias in WRF-27km, which improved dramatically in WRF-gray. It shows that higher model resolution and better simulation of large-scale atmospheric circulation also have considerable contributes to the improvement of monsoon rainfall simulation in WRF-gray, which will be discussed in details in the following sections. In addition, we can also find that the simulations at gray zone resolution (WRF-gray) can better capture the interannual variability of the monsoon rainfall amount than the coarse WRF simulations (WRF-27km). The rest of this paper will focus on the assessment of the ISM and MISO simulations in WRF-gray while both the MISO simulations in WRF-gray and WRF-27km will be compared to the observations in section 4.

3. Mean features of Indian Summer Monsoon

The large-scale atmospheric circulation and temporal-spatial patterns of the monsoon rainfall in WRF-gray are first assessed in this section. Fig. 3a and 3b show the 5-yr JJAS climatological mean 200-hPa winds and geopotential heights extracted from ERA-Interim and WRF-gray. During the summer monsoon, the upper troposphere (200 hPa) is characterized by a strong anti-cyclone over the Tibetan plateau and easterly winds over the Indian subcontinent. The model well captures the wind pattern and geopotential height in the upper troposphere, though the Tibetan high-pressure and easterly winds in WRF-gray are slightly stronger than that in ERA-Interim (Fig. 3b). At lower level (850-hPa), the model realistically simulates the geographical position and strength of Somali Jet over the Arabian Sea, with a slight overestimation of the wind speed (Fig. 3c and 3d). Moisture is transported by the strong low-level winds from the Arabian Sea to the Indian subcontinent. As a result, a precipitable

235 water maximum can be found over West Ghats and the Eastern coast of the Arabian Sea in both
236 in ERA-Interim and WRF-gray, though the precipitable water over the mountainous rages of
237 West Ghats in WRF-gray is a little higher than that in ERA-Interim. In addition, WRF-gray also
238 well captures the rain shadow downwind of the mountainous areas of central and southern India
239 where a slight dry bias can be noticed (Fig. 3d). The low-level southwesterly winds over the Bay
240 of Bengal in WRF-gray are stronger than that in ERA-Interim, which leads to an overestimation
241 in the precipitable water over the north tip of the Bay of Bengal, the west coast of Myanmar and
242 the foothills of Himalaya (Fig. 3d). A comparison of JJAS-averaged daily rainfall distribution
243 observed by TRMM with that simulated by WRF-gray is shown in Figs 3e and 3f. In general,
244 WRF-gray realistically captures the spatial pattern of the monsoon rainfall with the regional
245 rainfall maximums over West Ghats, central India, Himalaya foothills and the west coast of
246 Myanmar. Consistent with the biases shown in the low-level wind and precipitable water fields
247 (Fig. 3d), the simulated surface rainfall shows a dry bias over central India and a moist bias over
248 West Ghats, Himalaya foothills and the west coast of Myanmar (the Bay of Bengal). Similar
249 features can also been found in earlier RCM studies (e.g., Lucas-Picher et al., 2011; Rockel and
250 Geyer, 2008), which have shown that these biases can be explained by the way that surface
251 schemes cannot well simulate the land-sea pressure and temperature contrasts that driving the
252 monsoon dynamics and induce an overestimation of surface wind speed over oceans. This results
253 in an overestimation of the surface evaporation over the tropical oceans and excess precipitation
254 downstream over the mountain ranges of South-East Asia.

255 The Somali Jet over the Arabian Sea is a central figure of the Indian Summer Monsoon. Its
256 emergence is crucial in determining the onset precipitation over the Indian subcontinent (Ji and
257 Vernekar, 1997; Joseph and Sijikumar, 2004). Ajayamohan (2007) proposed an index to

represent the Kinetic Energy (KE) of Somali Jet (KELLJ), which is defined as the mean KE of winds at 850 hPa averaged over 50^{o}-65^{o}E and 5^{o}-15^{o}N (shown by the black box in Fig. 1). The same index is applied here to assess the strength of Somali Jet. The 5-yr temporal evolutions of KELLJ calculated from WRF-gray and WRF-27km are compared with that calculated from ERA-Interim in Fig. 4. In general, the simulations well capture the evolution of KELLJ in different years. Sudden increases in KE of Somali Jet in late May associated with the monsoon onsets are well reproduced in both WRF-gray and WRF-27km. The Somali Jet is stronger during the monsoon (JJAS) than in May and October, which leads to a stronger precipitation over the Indian subcontinent during the ISM. WRF-gray also well simulates the intraseasonal variation of KELLJ and the decrease of KE associated with the withdrawal of the monsoon in each year. Overall, the strength of Somali Jet in WRF-gray is slightly stronger than that in ERA-Interim, which is similar with the above analysis of Figs. 3c and 3d. However, the strength of Somali Jet in WRF-27km is much stronger when compared to WRF-gray and ERA-Interim. It is one of the reasons why there is a high moist bias of monsoon rainfall in WRF-27km. In general, the simulation at gray zone resolution can better capture the large scale atmospheric circulation of Indian summer monsoon than the coarser resolution simulation with cumulus scheme.

The evolution of surface rainfall averaged over the Indian subcontinent (shown by the blue polygon) from WRF-gray and WRF-27km is compared with that from TRMM observations (Fig. 5). The seasonal mean Indian monsoon rainfall for each year in TRMM, WRF-gray and WRF-27km has been given in each panel. Generally speaking, WRF-gray well captures the mean strength and intraseasonal variation of the monsoon rainfall. In these 5 years, the accumulated monsoonal rainfall amount over the Indian subcontinent is largest in 2010 (9.1 mm/day) and smallest in 2009 (7.1 mm/day). 2009 is also one of the most drought years in the past 3 decades.

281 Corresponding to the evolution of Somali Jet, rainfall over the Indian subcontinent begins to
282 increase from late May, reaches it maximum during JJAS and decreases again in late September
283 or early October, which are associated with the onsets and withdrawals of the ISM. The onset
284 and withdrawal of the ISM are well captured by WRF-gray in most years except the onset of the
285 2007 ISM in WRF-gray is later than that in TRMM observations. The main reason of the 2007
286 ISM later onset in WRF-gray is that the super cyclonic storm Gonu which induced strong
287 precipitation over the west India and had considerable influence on the onset of the 2007 ISM
288 (Najar and Salvekar, 2010) has not been well captured in the WRF simulation (the position of
289 Gonu has a southwest shift in WRF-gray, not shown here). The ISM also shows a strong ISO in
290 each year in the form of "active" and "break" spells of monsoon rainfall over the Indian
291 subcontinent. These "active" and "break" phases of ISM are closely related to the strengthening
292 and weakening of Somali Jet (Fig. 4). Despite the biases of the monsoon rainfall intensity, we
293 can find that WRF-gray well captures most "active" and "break" spells of 5-yr ISMs, which
294 gives us confidence that the MISO can be qualitatively simulated in the RCMs at gray zone
295 resolution. Compared to WRF-gray, the surface rainfall in WRF-27km shows a high moist bias
296 over the Indian subcontinent, which is consistent with the overprediction of the Somali Jet
297 strength shown in Fig. 4 and the analysis of seasonal mean rainfall in Fig. 2. Also, the
298 intraseasonal variation of monsoon rainfall is poorer simulated in WRF-27km when compared
299 with that in WRF-gray. For example, the "active" and "break" spells from August to September
300 in 2007 are well captured by WRF-gray while not simulated in WRF-27km. The 5-years
301 averaged correlation coefficient of precipitation between WRF-gray (WRF-27km) and TRMM
302 observations is 0.786 (0.714). These results show that the simulation at gray zone resolution can

303 better capture both the mean intensity and the intraseasonal variation of Indian summer monsoon
304 than the coarser resolution simulation using cumulus scheme.

305 The spatial distributions of monthly mean precipitation from TRMM and WRF-gray in 2007,
306 2009 and 2011 are compared in Figs 6, 7 and 8. Similar with the analysis of Fig.3, the model
307 well captures the rainfall centers over West Ghats, central Indian, Himalaya foothills and the
308 west coast of Myanmar during the summer monsoon seasons, with an overestimation of
309 precipitation over the west coast of Myanmar and Himalaya foothills due to the overprediction of
310 low-level wind over the Bay of Bangle. With high spatial resolution, WRF-gray is able to
311 capture the finer details of orographic precipitation over the mountainous rages (for example,
312 along the west coastline of the Indian subcontinent). In addition, the interannual variability of
313 monsoon rainfall is also well simulated in WRF-gray (Figs. 6, 7 and 8). In 2007, rainfall is very
314 weak over the Indian subcontinent in May though orographic precipitation can still be found over
315 the mountainous rages along the west coastline (Figs. 6a and 6g). Accompany with the onset of
316 the ISM and the enhancement of low-level winds over the Arabian Sea, precipitation over the
317 west coast of Indian subcontinent and its adjacent oceans increases dramatically in June (Figs. 6b
318 and 6h). In July, the precipitation center along the west coast of Indian subcontinent is still
319 apparent and the precipitation over central India is increased considerably (Figs. 6c and 6i).
320 Rainfall over Himalaya foothills and the west coast of Myanmar also reaches its strongest stage
321 in this month. In August, rainfall over central India and the west coast of Myanmar are still
322 strong while the precipitation near the Himalaya foothills is decreased (Figs. 6d and 6j). The
323 rainfall intensity over the entire monsoon region decreases continually in September (Figs. 6e
324 and 6k) and the precipitation over the Indian subcontinent becomes very weak in October (Figs.
325 6f and 6l), which represents the end of the monsoon season. When compared to 2007, the ISM in

2009 is dryer, especially over the Indian subcontinent (Fig. 7). The onset and withdrawal of the 2009 ISM over the Indian subcontinent are in June and September. The significant "break" spells of the 2009 ISM in June, August and September are well captured by WRF-gray (Figs. 5c, 7h, 7j and 7k). The evolution of monthly mean precipitation in 2011 (Fig. 8) is similar with that in 2007 (Fig. 6) with the rainfall over the central India reaches its strongest stage in August (Figs. 8d and 8j). In May 2011, an apparent moist bias of precipitation can be found over the Arabian Sea in WRF-gray, which is induced by the formation of an unreal tropical cyclone in the simulation. Generally speaking, WRF-gray is able to capture the spatial and temporal features of the ISM rainfall. Though apparent biases can still be found, the intensity and spatial pattern of monsoon rainfall in WRF-gray are verified well against the observations, especially over the Indian subcontinent.

4. Monsoon Intraseasonal Oscillations (MISO)

As mentioned in the Introduction, the MISO has fundamental influences on the seasonal mean, predictability and interannual variability of the ISM. Hence, the simulation of the MISO is very important for the credibility of the model in simulating the ISM. The section evaluates the ability of WRF-gray in simulating the MISO. MISO Phase composites of the surface rainfall and large-scale flows from WRF-gray are compared with that from the observations

4.1 Indices for the MISO

Using the developed nonlinear Laplacian spectral analysis (NLSA) technique (Giannakis and Majda, 2012b, a), Sabeerali et al. (2017) developed improved indices for real-time monitoring of the MISO. NLSA is a nonlinear data analysis technique that combines ideas from kernel methods

for harmonic analysis, delay embedding of dynamical systems and machine learning (Belkin and Niyogi, 2003; Packard et al., 1980; Sauer et al., 1991; Coifman and Lafon, 2006). Compared to the classical covariance-based approaches (for example Suhas et al., 2013; Krishnamurthy and Shukla, 2007), a key advantage of NLSA is that it is able to extract the spatiotemporal modes of variability spanning multiple timescales without requiring bandpass filtering or seasonal partitioning of the input data. Compared to the MISO indices based on the extend EOF (EEOF) and multichannel singular spectral analysis (MSSA), the NLSA-based MISO indices have improved timescale separation, higher memory and higher predictability. The MISO indices constructed by NLSA can better resolve the temporal and spatial characteristics of the MISO. For example, the NLSA-based MISO indices have better temporal phase coherence while maintaining the isolating ability of MISO from broad band dataset. It can better resolve the tilted structure of MISO convection and the associated atmospheric circulation pattern through phase composites and also explain more fractional variance over the ocean regions (Sabeerali et al., 2017).

In order to evaluate the MISO simulation in WRF-gray, the NLSA MISO indices are applied in this study to construct the phase composites of rainfall and atmospheric circulation from WRF-gray and the observations. Fig. 9 shows the daily evolution of the MISO in each year monitored by the two-dimensional phase space diagram constructed from the NLSA MISO indices. All indices are extracted from the TRMM observations. The 2D phase space of the NLSA MISO indices is divided into 8 phases to represent different phases of the MISO. The significant MISO event is defined as the instantaneous MISO whose amplitude is greater than 1.5 (shown by the black circle in Fig. 9). From Fig. 9, we can find that the MISO activity in 2007, 2008 and 2009 are much more significant than that in 2010 and 2011. The accumulated monsoon

372 rainfall amount over the Indian subcontinent is high in 2007 (8.8 mm/day), which also features
373 the strongest MISO activity (Fig. 9a). The following year, 2008, is also a moist year with strong
374 MISO activity which is from the end of June to the end of September (Fig. 9b). In 2009 (Fig. 9c),
375 a severe drought year, the MISO is weak during the early and late stages of the monsoon season
376 (June and September), but stronger in the midst of the monsoon season (July and August). The
377 amplitude of the MISO indices in 2010 and 2011 are much smaller, while significant MISO
378 events can still be found in most monsoon months (July, August and September) in 2011 (Fig.
379 9e).
380

381 **4.2 Phase composites of surface rainfall**

382 Fig. 10 shows the phase composites of daily surface rainfall anomalies (subtracted the mean
383 daily rainfall of 5-yr monsoon seasons) obtained from TRMM observation based on the NLSA
384 MISO indices. The phase composites are computed by averaging the significant MISO activities
385 in each phase space occurred in the 5-yr monsoon seasons. An apparent northeastward
386 propagation of the MISO can be found in the phase composites (from the phase 1 to the phase 8),
387 which corresponds to the anticlockwise rotation in the 2D phase space of the MISO indices (Fig.
388 9). Phase 1 shows the formation of enhanced rainfall anomalies over the tropic Indian Ocean (Fig.
389 10a). During this phase, rainfall over the Indian subcontinent is suppressed. The enhanced
390 rainfall anomalies over the tropic ocean become stronger and move toward the Indian
391 subcontinent in Phase 2 (Fig. 10b) and reach West Ghats and its adjoining oceans in Phase 3 and
392 Phase 4 (Figs. 10c and 10d). In Phase 3, precipitation over the Indian subcontinent is enhanced
393 while rainfall over the Bay of Bengal is suppressed (Fig. 10c). Rainfall over central India is
394 enhanced considerably in Phase 4 (Fig. 10d) and form into a northwest-southeast enhanced

rainfall line that stretches from the west coast of the Indian subcontinent to the south of the Indochina in Phase 5 (Fig. 10e). This enhanced rainfall line continually propagates to northeast in Phase 6 (Fig. 10f). In Phase 7, the enhanced rainfall anomalies can still be found over northwest India and west coast of Myanmar while the rainfall in south India is suppressed by the MISO. The total rainfall over the entire basin is weakest during Phase 8 with the rainfall anomalies are mostly negative over the inland regions of India (Fig. 10h). However, rainfall near Himalaya foothills begins to increase in this phase and reaches its maximum in Phase 1 (Fig. 10a). The phase composites of daily surface rainfall anomalies obtained from 5-yr TRMM observations in this study are similar to the 26-yr phase composites in Sabeerali et al. (2017), which shows that the 5-yr rainfall statistic reflects the climatological characteristics of the MISO.

Fig.11 presents the phase composites of daily surface rainfall anomalies obtained from WRF-gray. Despite differences in the intensity and location of rainfall anomalies, the MISO simulation in WRF-gray verified well against the TRMM observations. The fundamental features of rainfall anomalies in all 8 phases of the MISO are well captured by WRF-gray: for example, the northeastward propagation of the enhanced rainfall anomalies, the “active” and “break” phases of the monsoon rainfall over the Indian subcontinent, the northwest-southeast enhanced rainfall line in Phases 5 and 6, the increase of rainfall over Himalaya foothills in Phase 8 and Phase 1 and so on. Nonetheless, we also notice that the amplitude of the rainfall anomalies in WRF-gray is slightly larger than that in the TRMM observations, which reflects that the model simulated MISO is stronger than that in the satellite observations.

In order to evaluate to what extent the RCM at gray zone resolution can improve the simulation of the MISO, the phase composites of daily surface rainfall anomalies obtained from WRF-27km (Fig. 12) are also compared with that from the TRMM observations (Fig. 10) and

418 WRF-gray (Fig. 11) in this section. We can find that the amplitude of rainfall anomalies in
419 WRF-27km is much larger than that in WRF-gray and TRMM observations, which shows the
420 WRF-27km has larger systematic biases than WRF-gray in simulating the MISO intensity.
421 Though WRF-27km can also basically capture the "active" (Figs 12d, 12e and 12f) and "break"
422 (Figs. 12h, 12a and 12b) phases of the ISM, it shows a larger bias in the spatial-temporal
423 distributions of the rainfall anomalies during the different phases of the MISO than WRF-gray.
424 For example, the rainfall anomalies in Phase 1 and 2 (Figs. 12a and 12b) are shifted northward,
425 consistent with a faster development of the MISO cycle in the coarse resolution model. The
426 northwest-southeast enhanced rainfall line shown in TRMM observations and WRF-gray is not
427 clear in WRF-27km. This could be possibly due to deficiencies in how WRF-27km capture
428 stratiform rainfall, which would create a bias toward more patchy, deep convective events. The
429 increase of rainfall over Himalaya foothills from Phase 8 to Phase 1 has not been well simulated
430 in WRF-27km. Generally speaking, WRF-gray better simulates the MISO than WRF-27km, both
431 in the aspects of intensity and the spatial-temporal evolution.

432 Besides the phase composite, the evolutions of 10-day averaged daily surface rainfall
433 anomalies in WRF-gray and TRMM observations are also compared with each other to further
434 assess the credibility of WRF-gray in simulating the intraseasonal variability of the ISM. 10-day
435 evolutions of rainfall anomalies from 1 July to 10 August, 2009 in TRMM observations and
436 WRF-gray are shown in Fig. 13. During this period, the monsoon rainfall over the Indian
437 subcontinent turns from a strong "active" phase to a strong "break" phase (Fig. 5c). The rainfall
438 is enhanced over the west coast of the Indian subcontinent, central India and the Bay of Bengal
439 in the first ten days of July (Fig. 13a), which is similar with the combined features of Phases 4
440 and 5 (Figs. 10d and 10e). The enhanced rainfall anomalies form into a northwest-southeast line

441 in the middle of July (Fig. 13b), which corresponds to Phases 6. In the end of July, rainfall over
442 most area of the Indian subcontinent is suppressed while the rainfall anomalies over northwest
443 India and west coast of Myanmar are still positive (Fig. 13c). In early August, rainfall anomalies
444 over the entire Indian subcontinent turn to negative with rainfall over Himalaya foothills is
445 enhanced (Fig. 13d), which is similar to the combined features of Phases 8 and 1(Figs. 10h and
446 10a). Though small biases can be found in the simulated rainfall intensity and location, the
447 10-day evolutions of daily rainfall anomalies in WRF-gray verified well against the TRMM
448 observations (Figs. 13e-h), which again proves that the cloud-permitting RCM at gray zone
449 resolution is credible in simulating the MISO.
450
451 **4.3 Phase composites of atmospheric circulation**
452 During the different phases of the MISO, the large-scale flows and atmospheric conditions
453 also exhibit different behaviors (Raju et al., 2015; Goswami et al., 2003; Mukhopadhyay et al.,
454 2010). Fig. 14 shows the phase composites of 850-hPa wind and precipitable water anomalies
455 obtained from ERA-Interim. Consistent with the phase evolution of the enhanced daily rainfall
456 anomalies (Fig. 10), the precipitable water anomalies also show an apparent northeastward
457 propagation from Phase 1 (Fig. 14a) to Phase 8 (Fig. 14h), which corresponds to the
458 anticlockwise rotation in the 2D phase space of the MISO indices (Fig. 9). The major features of
459 the MISO active phase (Figs. 14f) are the formation of low pressure anomalies over northwest
460 and central India which is associated with the southward shifting of monsoon trough (Raju et al.,
461 2015). As a result, the strong westerly wind over the Arabian Sea and the Bay of Bengal also
462 enhanced dramatically during the active phase of the MISO, which transports more water vapor
463 from the oceans to the inland regions and leads to enhanced precipitable water anomalies over

464 the land. The strength of Somali Jet is also enhanced during the MISO active phase (Fig. 14f).
465 During the break phase of the MISO, on the other hand, high pressure anomalies can be found
466 over northwest and central India, which is associated with the northward shifting of monsoon
467 trough. The westerly wind over the Arabian Sea and Somali Jet are weakened during the break
468 phase (Figs. 14a), which lead to negative precipitation water and surface rainfall anomalies over
469 the Indian subcontinent. Fig. 15 shows the phase composites of 850-hPa wind anomalies and
470 precipitable water anomalies obtained from WRF-gray. We can find that WRF-gray well
471 produces the features of large-scale flow and precipitable water anomalies in different phases of
472 the MISO (Fig. 15), which shows that the cloud-permitting RCM at gray zone resolution can also
473 well capture the large-scale circulation features of the MISO. We should notice that, as the
474 rainfall anomalies shown in Fig. 11, the amplitudes of low-level wind and precipitable water
475 anomalies in WRF-gray (Fig. 15) are larger than that in ERA-Interim (Fig. 14), which implies
476 that the simulated MISO in WRF-gray is stronger than the real one.
477

478 **4.4 Sensitivity to initial dates**

479 While WRF-gray captures many aspects of the ISM and MISO qualitatively, quantitative
480 model biases are still apparent. These biases may induced by various reasons such as the choices
481 of surface scheme, the model domain size and the initial conditions which the dynamical systems
482 are highly sensitive to. The sensitivity of WRF-gray simulation to initial dates is further
483 investigated in this section. Fig. 16 shows the temporal evolutions of Somali Jet Strength (Fig.
484 16a), precipitation water (Fig. 16b) and precipitation (Fig. 16c) averaged over the Indian
485 subcontinent in the WRF simulations at gray zone resolution started from three different days
486 (WRF0420: blue lines, started from 0000 UTC 20 April; WRF0419: red lines, started from 0000

UTC 19 April; WRF0421: green lines, started from 0000 UTC 21 April) in 2007. Though all three WRF simulations are forced by the same lateral boundary conditions and the initial times are also close to each other, we can still find apparent differences of the simulated monsoon atmospheric circulation (Fig. 16a), humidity (Fig. 16b) and precipitation (Fig. 16c) in three experiments. In particular, in May, there exist apparent rainfall biases in WRF0419. However the onset of the ISM is better captured by WRF0419 than WRF0420 and WRF0421. The overprediction of monsoon rainfall from 15 September to 01 October in WRF0420 is considerably reduced in WRF0419 and WRF0421. Results show that the ISM and MISO simulations in RCM at gray zone resolution are sensitive to the initial conditions.

5. Summary and discussion

Simulations of the ISM by cloud-permitting WRF model at gray resolution (9 km) are evaluated in this study, with a particular emphasis on the credibility of the MISO simulation. The model is forced by ERA-Interim reanalysis for every year from 20 April to 30 October during 2007-2011. Model domain covers the entire Indian monsoon region which allows the systematic evolution of the ISM internal dynamics. Compared with the RCM at coarse resolution and using the cumulus parameterization scheme (WRF-27km), the systematic biases of monsoon rainfall climatology in the cloud-permitting RCM at gray zone resolution (WRF-gray) are reduced considerably. The interannual variability of the accumulated monsoon rainfall over the Indian subcontinent is also better captured in WRF-gray.

Results from WRF-gray are compared quantitatively with the reanalysis and long-term TRMM observations. In general, WRF-gray could reproduce the fundamental features of ISM reasonably well. The Tibetan high-pressure and easterly winds at 200 hPa in WRF-gray are slightly stronger

than that in ERA-Interim. The low-level southwesterly winds over the Bay of Bengal in WRF-gray is also stronger when compared to that in the reanalysis, which leads to an overprediction of precipitable water and surface rainfall over the west coast of Myanmar and Himalaya foothills in WRF-gray. The temporal evolutions of Somali jet and surface rainfall averaged over the Indian subcontinent are also well simulated in WRF-gray. The model captures most onsets, breaks and withdrawals of the ISMs, while the ISM onset in 2007 is later in WRF-gray than that in TRMM observation. Spatial distributions of monthly mean precipitation from TRMM and WRF-gray are further compared in the current study. Results show that WRF-gray could reproduce the spatial patterns of the monthly rainfall in each year and well capture the monsoon rainfall centers over West Ghats, central India, Himalaya foothills and the west coast of Myanmar. However, biases of rainfall intensity and position can still be found in WRF-gray, for example, the model simulates an unreal tropical cyclone over the Arabian Sea in May 2011.

Because the MISO has fundamental influences on the simulation and prediction of the ISM, the skill of WRF-gray in simulating the MISO is quantitatively assessed in this study. The NLSA MISO indices developed by Sabeerali et al. (2017) are applied in this study to construct the MISO phase composites of surface rainfall and atmospheric circulations from WRF-gray and observations. The enhanced rainfall anomalies show a clear northeastward propagation from the MISO Phases 1 to 8. WRF-gray well captures this northeastward propagation and also simulates the spatial distribution of rainfall anomalies during different phases of the MISO. The low-level westerly wind over the Arabian Sea and Somali jet are strengthened (weakened) during the active (break) phase of the MISO, which induces higher (lower) precipitable water and stronger (weaker) precipitation over the Indian subcontinent. These features can also be well reproduced

in WRF-gray, though the amplitude of rainfall, precipitable water and wind anomalies in WRF-gray are larger than that in observations. When compared with WRF-27km, the systematic biases in simulating the MISO have been reduced considerably in WRF-gray, which shows that the cloud-permitting RCM is able to improve the simulations of the MISO associated with the ISM.

While WRF-gray captures many aspects of the ISM and MISO qualitatively, quantitative model biases are still apparent. These biases may be induced by various reasons such as the initial conditions. More comprehensive investigation of the predictability of the ISO and MISO in RCM at gray zone resolution is deserved future studies.

Acknowledgements: Many thanks to Ajaya Ravindran and Sabeerali Cherumadanakadan Thelliyil for the multiple discussions that led to this paper. The author Xingchao Chen and Olivier Pauluis are supported by the New York University in Abu Dhabi Research Institute under grant G1102. The computations were carried out on the High Performance Computing resources at NYUAD. TRMM precipitation data were obtained from the NASA Goddard Space Flight Center. ECMWF reanalysis data were retrieved from the ECMWF Public Datasets web interface (http://apps.ecmwf.int/datasets/). WRF output can be made accessible by contacting xzc55@psu.edu.

REFERENCES

Ajayamohan, R. S., and Goswami, B. N.: Potential predictability of the Asian summer monsoon on monthly and seasonal time scales, Meteorology and Atmospheric Physics, 84, 83-100, 10.1007/s00703-002-0576-4, 2003.

Ajayamohan, R. S.: Simulation of South-Asian Summer Monsoon in a GCM, Pure and Applied Geophysics, 164, 2117-2140, 10.1007/s00024-007-0249-9, 2007.

Ajayamohan, R. S., Khouider, B., and Majda, A. J.: Simulation of monsoon intraseasonal oscillations in a coarse-resolution aquaplanet GCM, Geophys. Res. Lett., 41, 5662-5669, 10.1002/2014GL060662, 2014.

Belkin, M., and Niyogi, P.: Laplacian Eigenmaps for dimensionality reduction and data representation, Neural Comput., 15, 1373-1396, 10.1162/089976603321780317, 2003.

Betts, A. K., and Miller, M. J.: A new convective adjustment scheme. Part II: Single column tests using GATE wave, BOMEX, ATEX and arctic air-mass data sets, Q. J. R. Meteorol. Soc., 112, 693-709, 10.1002/qj.49711247308, 1986.

Bhaskaran, B., Mitchell, J. F. B., Lavery, J. R., and Lal, M.: Climatic response of the Indian subcontinent to doubled CO2 concentrations, Int. J. Climatol., 15, 873-892, 10.1002/joc.3370150804, 1995.

Bhaskaran, B., Jones, R. G., Murphy, J. M., and Noguer, M.: Simulations of the Indian summer monsoon using a nested regional climate model: domain size experiments, Climate Dynam., 12, 573-587, 10.1007/bf00216267, 1996.

Bhaskaran, B., Murphy, J. M., and Jones, R. G.: Intraseasonal Oscillation in the Indian Summer Monsoon Simulated by Global and Nested Regional Climate Models, Mon. Wea. Rev., 126, 3124-3134, 10.1175/1520-0493(1998)126<3124:ioitis>2.0.co;2, 1998.

Bollasina, M. A.: Hydrology: Probing the monsoon pulse, Nature Clim. Change, 4, 422-423, 10.1038/nclimate2243, 2014.

Bryan, G. H., Wyngaard, J. C., and Fritsch, J. M.: Resolution Requirements for the Simulation of Deep Moist Convection, Mon. Wea. Rev., 131, 2394-2416, 10.1175/1520-0493(2003)131<2394:rrftso>2.0.co;2, 2003.

Chatterjee, P., and Goswami, B. N.: Structure, genesis and scale selection of the tropical quasi-biweekly mode, Q. J. R. Meteorol. Soc., 130, 1171-1194, 10.1256/qj.03.133, 2004.

Chen, F., and Dudhia, J.: Coupling an Advanced Land Surface–Hydrology Model with the Penn State–NCAR MM5 Modeling System. Part I: Model Implementation and Sensitivity, Mon. Wea. Rev., 129, 569-585, 10.1175/1520-0493(2001)129<0569:caalsh>2.0.co;2, 2001.

Chen, G.-S., Liu, Z., Clemens, S. C., Prell, W. L., and Liu, X.: Modeling the time-dependent response of the Asian summer monsoon to obliquity forcing in a coupled GCM: a PHASEMAP sensitivity experiment, Climate Dynam., 36, 695-710, 10.1007/s00382-010-0740-3, 2011.

Coifman, R. R., and Lafon, S.: Diffusion maps, Applied and Computational Harmonic Analysis, 21, 5-30, https://doi.org/10.1016/j.acha.2006.04.006, 2006.

Das, S., Mitra, A. K., Iyengar, G. R., and Mohandas, S.: Comprehensive test of different cumulus parameterization schemes for the simulation of the Indian summer monsoon, Meteorology and Atmospheric Physics, 78, 227-244, 10.1007/s703-001-8176-1, 2001.

Dash, S. K., Shekhar, M. S., and Singh, G. P.: Simulation of Indian summer monsoon circulation and rainfall using RegCM3, Theoretical and Applied Climatology, 86, 161-172, 10.1007/s00704-006-0204-1, 2006.

Dee, D. P., Uppala, S. M., Simmons, A. J., Berrisford, P., Poli, P., Kobayashi, S., Andrae, U., Balmaseda, M. A., Balsamo, G., Bauer, P., Bechtold, P., Beljaars, A. C. M., van de Berg, L., Bidlot, J., Bormann, N., Delsol, C., Dragani, R., Fuentes, M., Geer, A. J., Haimberger, L., Healy, S. B., Hersbach, H., Hólm, E. V., Isaksen, L., Kållberg, P., Köhler, M., Matricardi, M., McNally, A. P., Monge-Sanz, B. M., Morcrette, J. J., Park, B. K., Peubey, C., de Rosnay, P., Tavolato, C., Thépaut, J. N., and Vitart, F.: The ERA-Interim reanalysis: configuration and performance of the data assimilation system, Q. J. R. Meteorol. Soc., 137, 553-597, 10.1002/qj.828, 2011.

Giannakis, D., and Majda, A. J.: Nonlinear Laplacian spectral analysis for time series with intermittency and low-frequency variability, Proceedings of the National Academy of Sciences, 109, 2222-2227, 10.1073/pnas.1118984109, 2012a.

Giannakis, D., and Majda, A. J.: Comparing low-frequency and intermittent variability in comprehensive climate models through nonlinear Laplacian spectral analysis, Geophys. Res. Lett., 39, n/a-n/a, 10.1029/2012GL051575, 2012b.

606 Giorgi, F.: Regional climate modeling: Status and perspectives, J. Phys. IV France, 139, 101-118, 2006.
607 Goswami, B.: Dynamical predictability of seasonal monsoon rainfall: Problems and prospects,
608 PROCEEDINGS-INDIAN NATIONAL SCIENCE ACADEMY PART A, 60, 101-101, 1994.
609 Goswami, B. B., and Goswami, B. N.: A road map for improving dry-bias in simulating the South Asian monsoon
610 precipitation by climate models, Climate Dynam., 1-10, 10.1007/s00382-016-3439-2, 2016.
611 Goswami, B. N., and Ajayamohan, R. S.: Intraseasonal Oscillations and Interannual Variability of the Indian Summer
612 Monsoon, J. Climate, 14, 1180-1198, 10.1175/1520-0442(2001)014<1180:ioaivo>2.0.co;2, 2001.
613 Goswami, B. N., Ajayamohan, R. S., Xavier, P. K., and Sengupta, D.: Clustering of synoptic activity by Indian summer
614 monsoon intraseasonal oscillations, Geophys. Res. Lett., 30, n/a-n/a, 10.1029/2002GL016734, 2003.
615 Grell, G. A., and Dévényi, D.: A generalized approach to parameterizing convection combining ensemble and data
616 assimilation techniques, Geophys. Res. Lett., 29, 38-31-38-34, 10.1029/2002GL015311, 2002.
617 Hong, S.-Y., Noh, Y., and Dudhia, J.: A New Vertical Diffusion Package with an Explicit Treatment of Entrainment
618 Processes, Mon. Wea. Rev., 134, 2318-2341, 10.1175/mwr3199.1, 2006.
619 Hu, X.-M., Nielsen-Gammon, J. W., and Zhang, F.: Evaluation of Three Planetary Boundary Layer Schemes in the
620 WRF Model, J. Appl. Meteor. Climatol., 49, 1831-1844, 10.1175/2010jamc2432.1, 2010.
621 Huffman, G. J., Adler, R. F., Morrissey, M. M., Bolvin, D. T., Curtis, S., Joyce, R., McGavock, B., and Susskind, J.: Global
622 Precipitation at One-Degree Daily Resolution from Multisatellite Observations, Journal of Hydrometeorology, 2,
623 36-50, 10.1175/1525-7541(2001)002<0036:gpaodd>2.0.co;2, 2001.
624 Iacono, M. J., Delamere, J. S., Mlawer, E. J., Shephard, M. W., Clough, S. A., and Collins, W. D.: Radiative forcing by
625 long-lived greenhouse gases: Calculations with the AER radiative transfer models, J. Geophys. Res. Atmos., 113,
626 n/a-n/a, 10.1029/2008JD009944, 2008.
627 Jain, S. K., and Kumar, V.: Trend analysis of rainfall and temperature data for India, Current Science(Bangalore), 102,
628 37-49, 2012.
629 Janjić, Z. I.: The Step-Mountain Eta Coordinate Model: Further Developments of the Convection, Viscous Sublayer,
630 and Turbulence Closure Schemes, Mon. Wea. Rev., 122, 927-945,
631 10.1175/1520-0493(1994)122<0927:tsmecm>2.0.co;2, 1994.
632 Ji, Y., and Vernekar, A. D.: Simulation of the Asian Summer Monsoons of 1987 and 1988 with a Regional Model
633 Nested in a Global GCM, J. Climate, 10, 1965-1979, 10.1175/1520-0442(1997)010<1965:sotasm>2.0.co;2, 1997.
634 Jiang, X., Li, T., and Wang, B.: Structures and Mechanisms of the Northward Propagating Boreal Summer
635 Intraseasonal Oscillation, J. Climate, 17, 1022-1039, 10.1175/1520-0442(2004)017<1022:samotn>2.0.co;2, 2004.
636 Joseph, P. V., and Sijikumar, S.: Intraseasonal Variability of the Low-Level Jet Stream of the Asian Summer Monsoon,
637 J. Climate, 17, 1449-1458, 10.1175/1520-0442(2004)017<1449:ivotlj>2.0.co;2, 2004.
638 Kain, J. S.: The Kain–Fritsch Convective Parameterization: An Update, J. Appl. Meteorol., 43, 170-181,
639 10.1175/1520-0450(2004)043<0170:tkcpau>2.0.co;2, 2004.
640 Kikuchi, K., Wang, B., and Kajikawa, Y.: Bimodal representation of the tropical intraseasonal oscillation, Climate
641 Dynam., 38, 1989-2000, 10.1007/s00382-011-1159-1, 2012.
642 Kishore, P., Jyothi, S., Basha, G., Rao, S. V. B., Rajeevan, M., Velicogna, I., and Sutterley, T. C.: Precipitation
643 climatology over India: validation with observations and reanalysis datasets and spatial trends, Climate Dynam., 46,
644 541-556, 10.1007/s00382-015-2597-y, 2016.
645 Klemp, J. B., Dudhia, J., and Hassiotis, A. D.: An Upper Gravity-Wave Absorbing Layer for NWP Applications, Mon.
646 Wea. Rev., 136, 3987-4004, 10.1175/2008mwr2596.1, 2008.
647 Kolusu, S., Prasanna, V., and Preethi, B.: Simulation of Indian summer monsoon intra-seasonal oscillations using
648 WRF regional atmospheric model, International Journal of Earth and Atmospheric Science, 1, 35-53, 2014.
649 Krishnamurthy, V., and Shukla, J.: Intraseasonal and Seasonally Persisting Patterns of Indian Monsoon Rainfall, J.
650 Climate, 20, 3-20, 10.1175/jcli3981.1, 2007.
651 Krishnamurti, T. N., and Bhalme, H. N.: Oscillations of a Monsoon System. Part I. Observational Aspects, J. Atmos.
652 Sci., 33, 1937-1954, 10.1175/1520-0469(1976)033<1937:ooamsp>2.0.co;2, 1976.
653 Lau, N.-C., and Ploshay, J. J.: Simulation of Synoptic- and Subsynoptic-Scale Phenomena Associated with the East
654 Asian Summer Monsoon Using a High-Resolution GCM, Mon. Wea. Rev., 137, 137-160, 10.1175/2008mwr2511.1,
655 2009.
656 Lau, W. K.-M., and Waliser, D. E.: Intraseasonal variability in the atmosphere-ocean climate system, Springer Science
657 & Business Media, 2011.
658 Lee, J.-Y., Wang, B., Wheeler, M. C., Fu, X., Waliser, D. E., and Kang, I.-S.: Real-time multivariate indices for the

boreal summer intraseasonal oscillation over the Asian summer monsoon region, Climate Dynam., 40, 493-509, 10.1007/s00382-012-1544-4, 2013.
Lim, K.-S. S., and Hong, S.-Y.: Development of an Effective Double-Moment Cloud Microphysics Scheme with Prognostic Cloud Condensation Nuclei (CCN) for Weather and Climate Models, Mon. Wea. Rev., 138, 1587-1612, 10.1175/2009mwr2968.1, 2010.
Lin, R., Zhou, T., and Qian, Y.: Evaluation of Global Monsoon Precipitation Changes based on Five Reanalysis Datasets, J. Climate, 27, 1271-1289, 10.1175/jcli-d-13-00215.1, 2014.
Lucas-Picher, P., Christensen, J. H., Saeed, F., Kumar, P., Asharaf, S., Ahrens, B., Wiltshire, A. J., Jacob, D., and Hagemann, S.: Can regional climate models represent the Indian monsoon?, Journal of Hydrometeorology, 12, 849-868, 2011.
Mukhopadhyay, P., Taraphdar, S., Goswami, B., and Krishnakumar, K.: Indian summer monsoon precipitation climatology in a high-resolution regional climate model: Impacts of convective parameterization on systematic biases, Wea. Forecasting, 25, 369-387, 2010.
Najar, K. A. A., and Salvekar, P. S.: Understanding the Tropical Cyclone Gonu, in: Indian Ocean Tropical Cyclones and Climate Change, edited by: Charabi, Y., Springer Netherlands, Dordrecht, 359-369, 2010.
Oouchi, K., Noda, A. T., Satoh, M., Wang, B., Xie, S.-P., Takahashi, H. G., and Yasunari, T.: Asian summer monsoon simulated by a global cloud-system-resolving model: Diurnal to intra-seasonal variability, Geophys. Res. Lett., 36, n/a-n/a, 10.1029/2009GL038271, 2009.
Packard, N. H., Crutchfield, J. P., Farmer, J. D., and Shaw, R. S.: Geometry from a Time Series, Physical Review Letters, 45, 712-716, 1980.
Pauluis, O., and Garner, S.: Sensitivity of Radiative–Convective Equilibrium Simulations to Horizontal Resolution, J. Atmos. Sci., 63, 1910-1923, 10.1175/jas3705.1, 2006.
Pleim, J. E.: A Combined Local and Nonlocal Closure Model for the Atmospheric Boundary Layer. Part I: Model Description and Testing, J. Appl. Meteor. Climatol., 46, 1383-1395, 10.1175/jam2539.1, 2007.
Prein, A. F., Langhans, W., Fosser, G., Ferrone, A., Ban, N., Goergen, K., Keller, M., Tölle, M., Gutjahr, O., Feser, F., Brisson, E., Kollet, S., Schmidli, J., van Lipzig, N. P. M., and Leung, R.: A review on regional convection-permitting climate modeling: Demonstrations, prospects, and challenges, Rev. Geophys., 53, 323-361, 10.1002/2014RG000475, 2015.
Rajendran, K., and Kitoh, A.: Indian summer monsoon in future climate projection by a super high-resolution global model, Current Science (00113891), 95, 1560-1569, 2008.
Raju, A., Parekh, A., Chowdary, J. S., and Gnanaseelan, C.: Assessment of the Indian summer monsoon in the WRF regional climate model, Climate Dynam., 44, 3077-3100, 10.1007/s00382-014-2295-1, 2015.
Ramu, D. A., Sabeerali, C. T., Chattopadhyay, R., Rao, D. N., George, G., Dhakate, A. R., Salunke, K., Srivastava, A., and Rao, S. A.: Indian summer monsoon rainfall simulation and prediction skill in the CFSv2 coupled model: Impact of atmospheric horizontal resolution, J. Geophys. Res. Atmos., 121, 2205-2221, 10.1002/2015JD024629, 2016.
Ratnam, J. V., and Kumar, K. K.: Sensitivity of the Simulated Monsoons of 1987 and 1988 to Convective Parameterization Schemes in MM5, J. Climate, 18, 2724-2743, 10.1175/jcli3390.1, 2005.
Rockel, B., and Geyer, B.: The performance of the regional climate model CLM in different climate regions, based on the example of precipitation, Meteorologische Zeitschrift, 17, 487-498, 2008.
Sabeerali, C. T., Rao, S. A., Ajayamohan, R. S., and Murtugudde, R.: On the relationship between Indian summer monsoon withdrawal and Indo-Pacific SST anomalies before and after 1976/1977 climate shift, Climate Dynam., 39, 841-859, 10.1007/s00382-011-1269-9, 2012.
Sabeerali, C. T., Ajayamohan, R. S., Giannakis, D., and Majda, A. J.: Extraction and prediction of indices for monsoon intraseasonal oscillations: an approach based on nonlinear Laplacian spectral analysis, Climate Dynam., 1-20, 10.1007/s00382-016-3491-y, 2017.
Saeed, F., Hagemann, S., and Jacob, D.: A framework for the evaluation of the South Asian summer monsoon in a regional climate model applied to REMO, Int. J. Climatol., 32, 430-440, 10.1002/joc.2285, 2012.
Samala, B. K., C, N., Banerjee, S., Kaginalkar, A., and Dalvi, M.: Study of the Indian summer monsoon using WRF–ROMS regional coupled model simulations, Atmospheric Science Letters, 14, 20-27, 10.1002/asl2.409, 2013.
Sauer, T., Yorke, J. A., and Casdagli, M.: Embedology, Journal of Statistical Physics, 65, 579-616, 10.1007/bf01053745, 1991.
Shi, J. J., Tao, W.-K., Matsui, T., Cifelli, R., Hou, A., Lang, S., Tokay, A., Wang, N.-Y., Peters-Lidard, C., Skofronick-Jackson, G., Rutledge, S., and Petersen, W.: WRF Simulations of the 20–22 January 2007 Snow Events

over Eastern Canada: Comparison with In Situ and Satellite Observations, J. Appl. Meteor. Climatol., 49, 2246-2266, 10.1175/2010jamc2282.1, 2010.
Sikka, D. R., and Gadgil, S.: On the Maximum Cloud Zone and the ITCZ over Indian, Longitudes during the Southwest Monsoon, Mon. Wea. Rev., 108, 1840-1853, 10.1175/1520-0493(1980)108<1840:OTMCZA>2.0.CO;2, 1980.
Skamarock, W., Klemp, J., Dudhia, J., Gill, D., Barker, D., Duda, M., Huang, X., Wang, W., and Powers, J.: A Description of the Advanced Research WRF Version 3 (2008) NCAR Technical Note, Boulder, CO, 2008.
Srinivas, C. V., Hariprasad, D., Bhaskar Rao, D. V., Anjaneyulu, Y., Baskaran, R., and Venkatraman, B.: Simulation of the Indian summer monsoon regional climate using advanced research WRF model, Int. J. Climatol., 33, 1195-1210, 10.1002/joc.3505, 2013.
Suhas, E., Neena, J. M., and Goswami, B. N.: An Indian monsoon intraseasonal oscillations (MISO) index for real time monitoring and forecast verification, Climate Dynam., 40, 2605-2616, 10.1007/s00382-012-1462-5, 2013.
Vernekar, A. D., and Ji, Y.: Simulation of the Onset and Intraseasonal Variability ofTwo Contrasting Summer Monsoons, J. Climate, 12, 1707-1725, 10.1175/1520-0442(1999)012<1707:sotoai>2.0.co;2, 1999.
Wang, S., Sobel, A. H., Zhang, F., Sun, Y. Q., Yue, Y., and Zhou, L.: Regional Simulation of the October and November MJO Events Observed during the CINDY/DYNAMO Field Campaign at Gray Zone Resolution, J. Climate, 28, 2097-2119, 10.1175/jcli-d-14-00294.1, 2015.
Yasunari, T.: Structure of an Indian Summer Monsoon System with around 40-Day Period, Journal of the Meteorological Society of Japan. Ser. II, 59, 336-354, 1981.

Figures

Figure 1. Model domain used in the WRF simulations with topography (gray scales) and coastlines (red lines). The black box shows the climatic zone used for the calculation of KELLF index and the blue polygon shows the Indian subcontinent.

Figure 2. Averaged daily rainfall over the Indian subcontinent for JJAS in different years from TRMM observation (blue bars), WRF-gray (green bars) and WRF-27km (yellow bars).

Figure 3. 5-yr mean monsoon (JJAS) winds (vectors) and geopotential heights (red contours) at 200-hPa from (a) ERA-Interim and (b) WRF-gray; winds (vectors) and precipitable water (color shadings) at 850-hPa from (c) ERA-Interim and (d) WRF-gray; daily surface precipitation (color shadings) from (e) TRMM and (f) WRF-gray. Topography is shown by the black contours starts at 500m with a 1000-m interval.

Figure 4. Temporal evolution of KELLF indices in (a) 2007; (b) 2008; (c) 2009; (d) 2010 and (e) 2011 from ERA-Interim (black lines), WRF-gray (blue lines) and WRF-27km (red lines). A 5-day moving average is applied to the time series.

Figure 5. Temporal evolution of daily surface rainfall averaged over the Indian subcontinent in (a) 2007; (b) 2008; (c) 2009; (d) 2010 and (e) 2011 from TRMM (black lines), WRF-gray (blue lines) and WRF-27km (red lines). A 5-day moving average is applied to the time series. The seasonal mean (June to September) of daily surface rainfall amounts averaged over the Indian subcontinent from TRMM (black), WRF-gray (blue) and WRF-27km (red) are also shown in the figure.

Figure 6. Spatial distributions of averaged daily surface precipitation from May to October in year 2007 derived from (a-f) TRMM and (g-l) WRF-gray.

Figure 7. Spatial distributions of averaged daily surface precipitation from May to October in

755 year 2009 derived from (a-f) TRMM and (g-l) WRF-gray.

756 Figure 8. Spatial distributions of averaged daily surface precipitation from May to October in
757 year 2011 derived from (a-f) TRMM and (g-l) WRF-gray.

758 Figure 9. 2D phase space diagrams for the NLSA MISO indices in years: (a) 2007, (b) 2008,
759 (c) 2009, (d) 2010 and (e) 2011. An anticlockwise propagation from the phase 1 represents
760 MISO's northward propagation. The circle centered at the origin has radius equal to 1.5, which is
761 the threshold for identification of significant MISO events.

762 Figure 10. Phase composites of daily surface rainfall anomalies obtained from TRMM (Figure
763 a-h: phase 1 to 8).

764 Figure 11. Phase composites of daily surface rainfall anomalies obtained from WRF-gray
765 (Figure a-h: phase 1 to 8).

766 Figure 12. Phase composites of daily surface rainfall anomalies obtained from WRF-27km
767 (Figure a-h: phase 1 to 8).

768 Figure 13. Spatial distributions of 10-day averaged daily surface rainfall anomalies in (a, e)
769 1-10 July, (d, f) 11-20 July, (c, g) 21-31 July and (d, h) 01-10 August, 2009 derived from TRMM
770 (left panels) and WRF-gray (right panels).

771 Figure 14. Phase composites of 850-hPa wind and precipitable water anomalies obtained from
772 ERA-Interim (Figure a-h: phase 1 to 8).

773 Figure 15. Phase composites of 850-hPa wind and precipitable water anomalies obtained from
774 WRF-gray (Figure a-h: phase 1 to 8).

775 Figure 16. Temporal evolutions of (a) KELLF indices, (b) precipitable water averaged over
776 the Indian subcontinent and (c) daily surface precipitation averaged over the Indian subcontinent
777 in year 2007 from ERA-Interim/TRMM (black lines), WRF-gray simulation starts from April 20

778 (blue lines, control run), WRF-gray simulation starts from April 19 (red lines) and WRF-gray
779 simulation starts from April 21 (green lines).
780

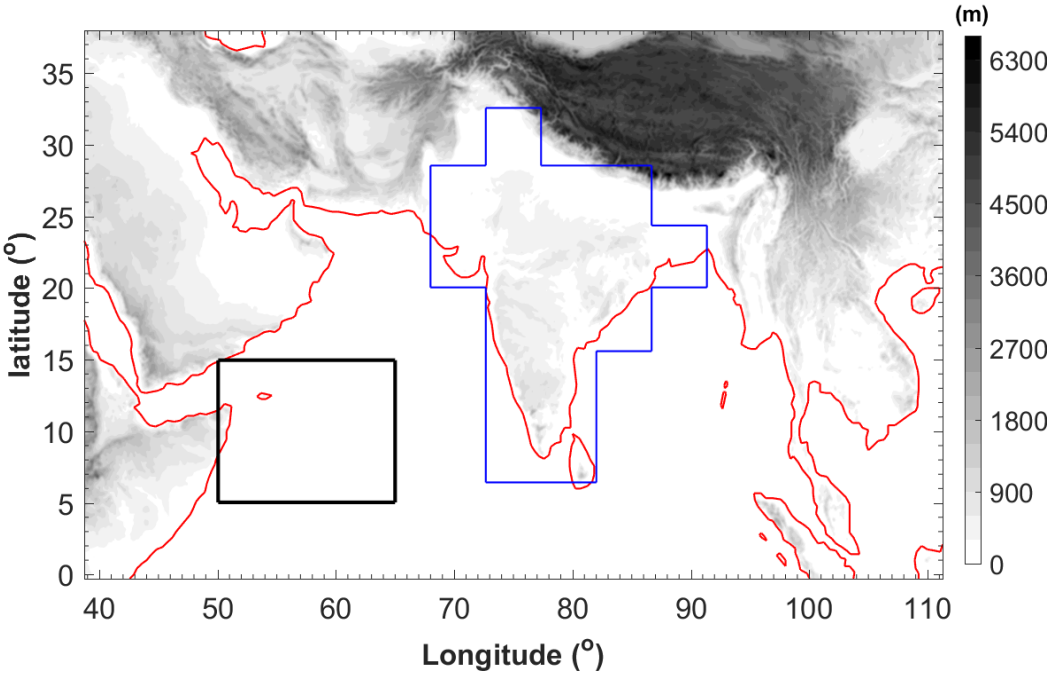

Figure 1. Model domain used in the WRF simulations with topography (gray scales) and coastlines (red lines). The black box shows the climatic zone used for the calculation of KELLF index and the blue polygon shows the Indian subcontinent.

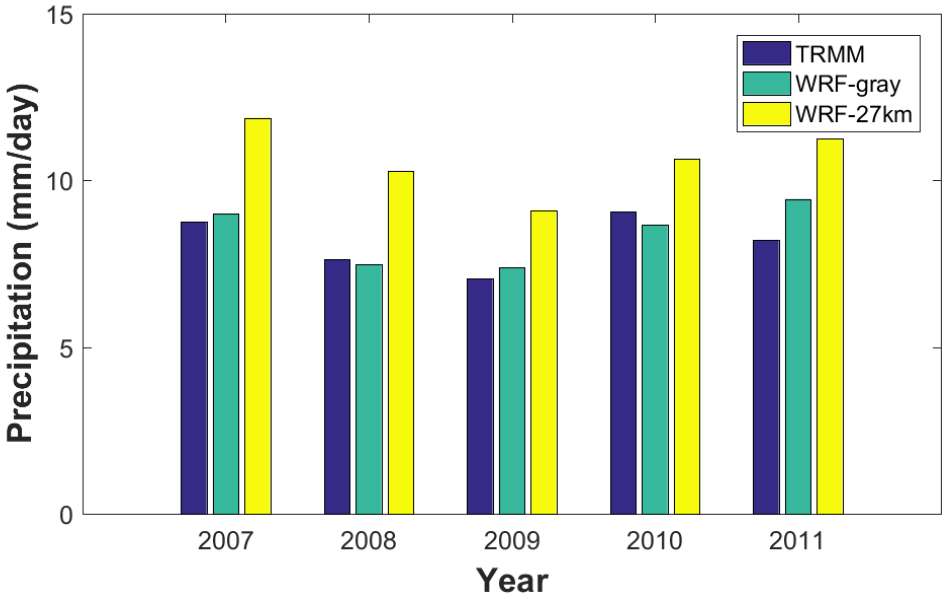

Figure 2. Averaged daily rainfall over the Indian subcontinent for JJAS in different years from TRMM observation (blue bars), WRF-gray (green bars) and WRF-27km (yellow bars).

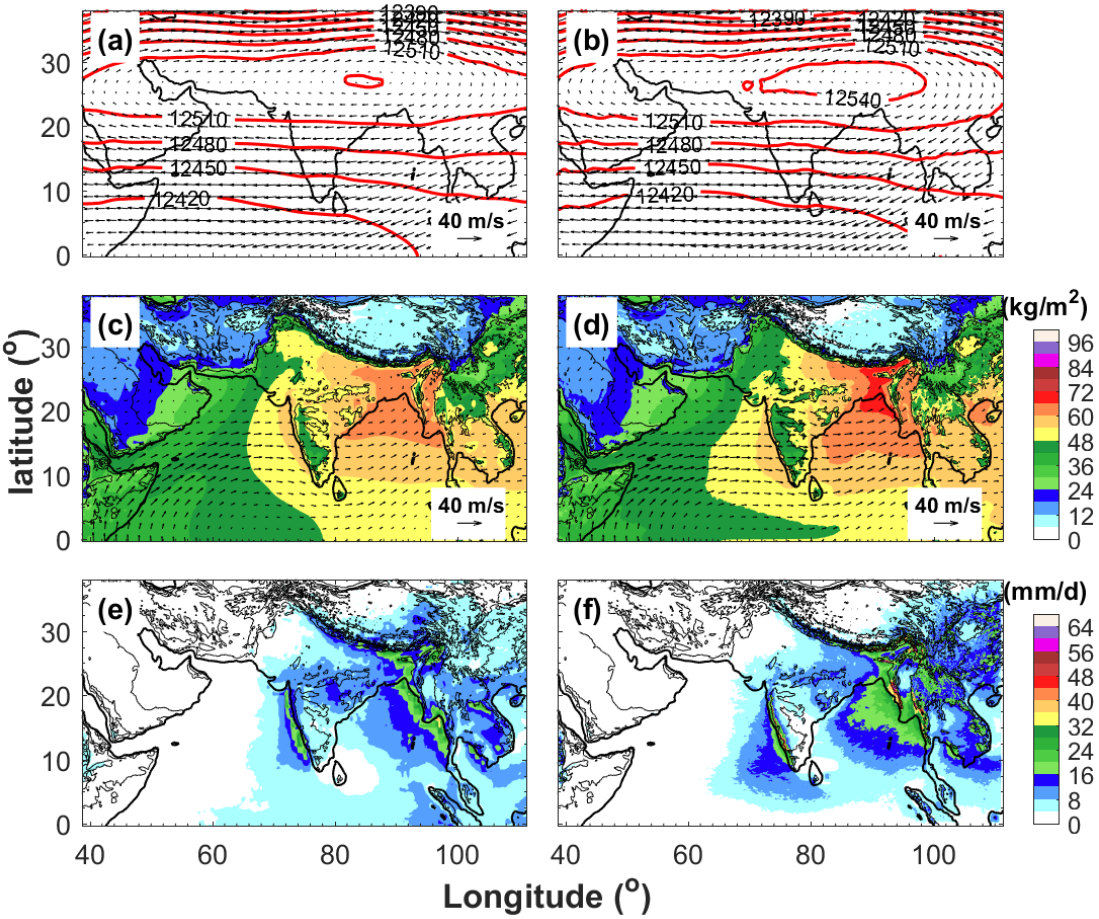

Figure 3. 5-yr mean monsoon (JJAS) winds (vectors) and geopotential heights (red contours) at 200-hPa from (a) ERA-Interim and (b) WRF-gray; winds (vectors) and precipitable water (color shadings) at 850-hPa from (c) ERA-Interim and (d) WRF-gray; daily surface precipitation (color shadings) from (e) TRMM and (f) WRF-gray. Topography is shown by the black contours starts at 500m with a 1000-m interval.

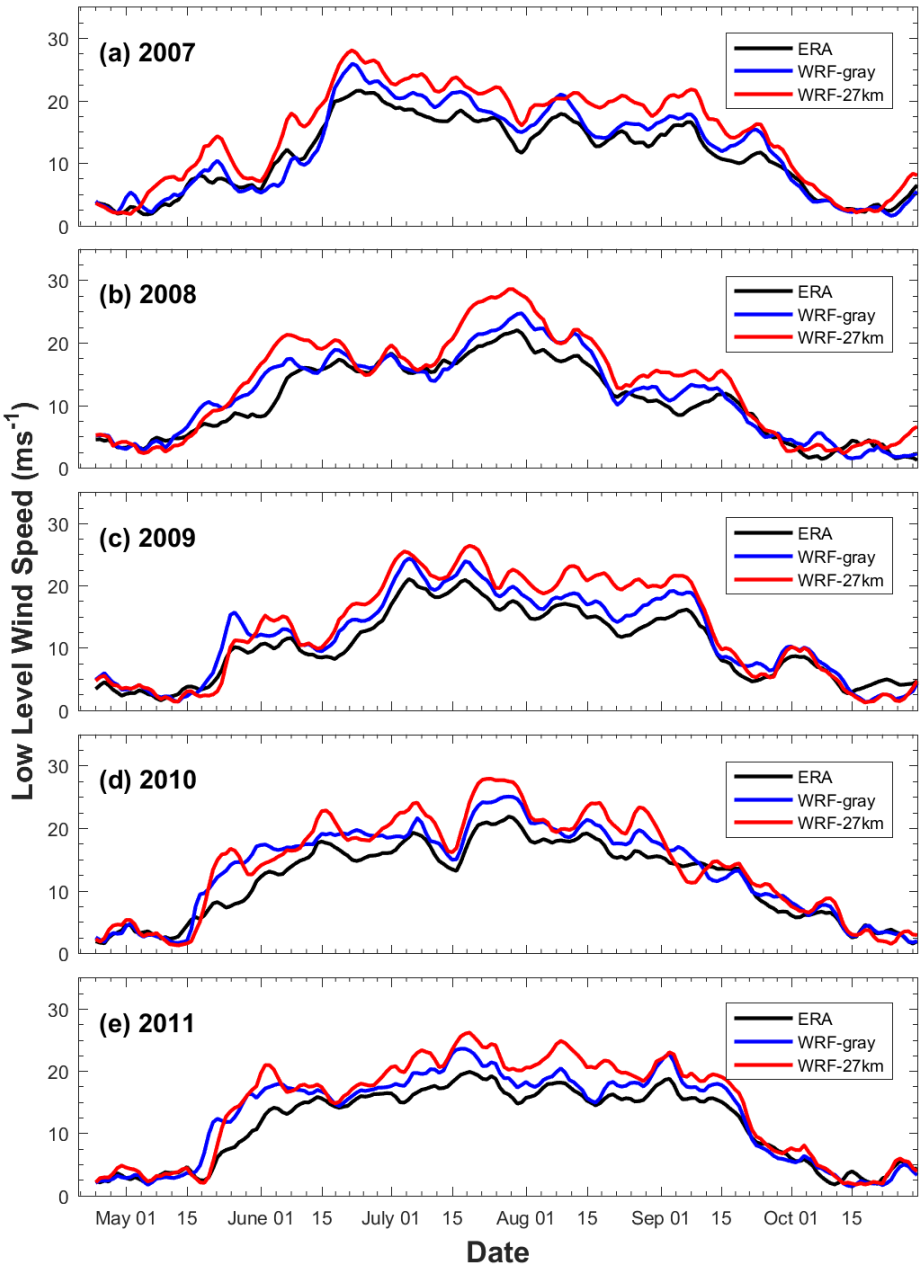

796
797 Figure 4. Temporal evolution of KELLF indices in (a) 2007; (b) 2008; (c) 2009; (d) 2010 and (e) 2011 from
798 ERA-Interim (black lines), WRF-gray (blue lines) and WRF-27km (red lines). A 5-day moving average is applied
799 to the time series.
800
801

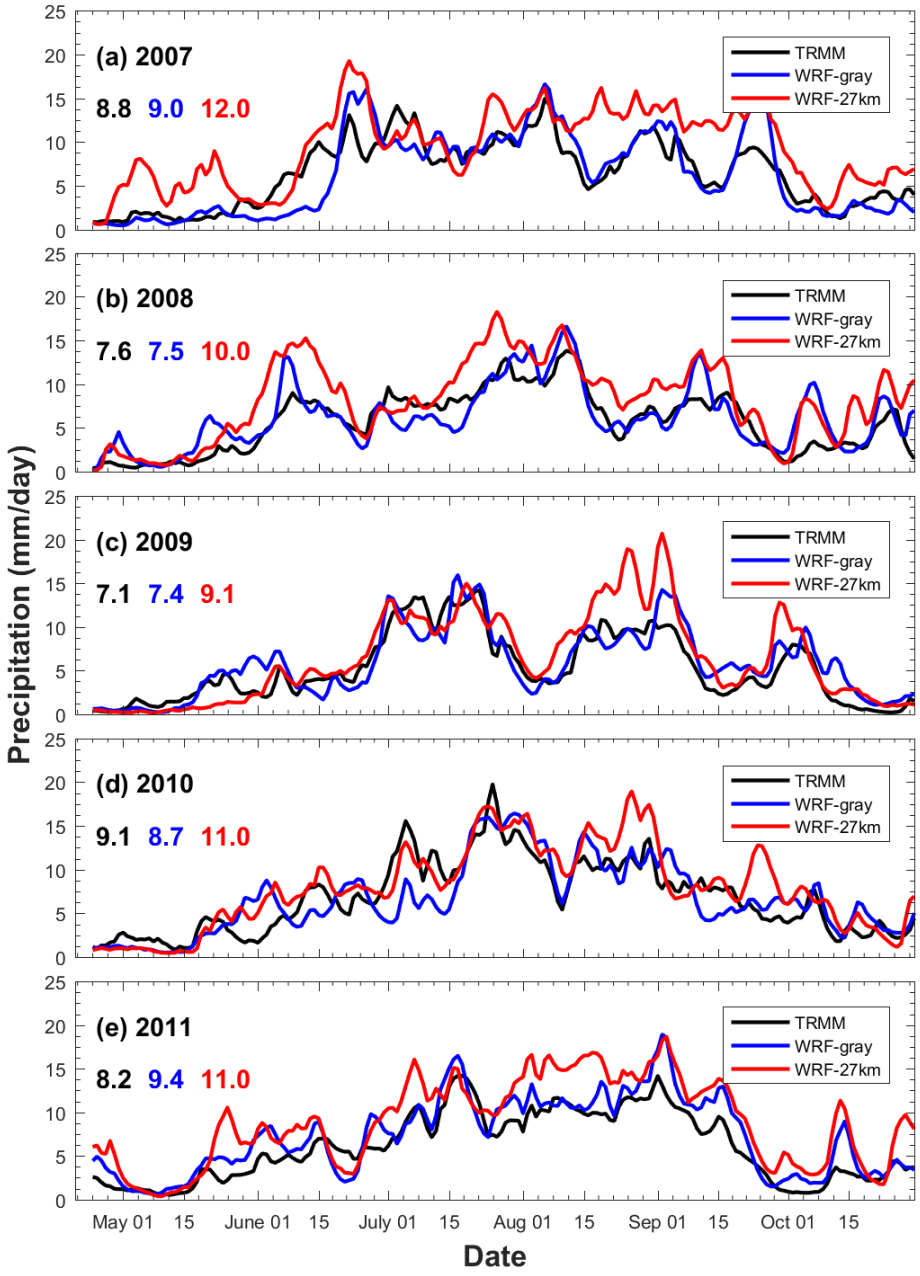

Figure 5. Temporal evolution of daily surface rainfall averaged over the Indian subcontinent in (a) 2007; (b) 2008; (c) 2009; (d) 2010 and (e) 2011 from TRMM (black lines), WRF-gray (blue lines) and WRF-27km (red lines). A 5-day moving average is applied to the time series. The seasonal mean (June to September) of daily surface rainfall amounts averaged over the Indian subcontinent from TRMM (black), WRF-gray (blue) and WRF-27km (red) are also shown in the figure.

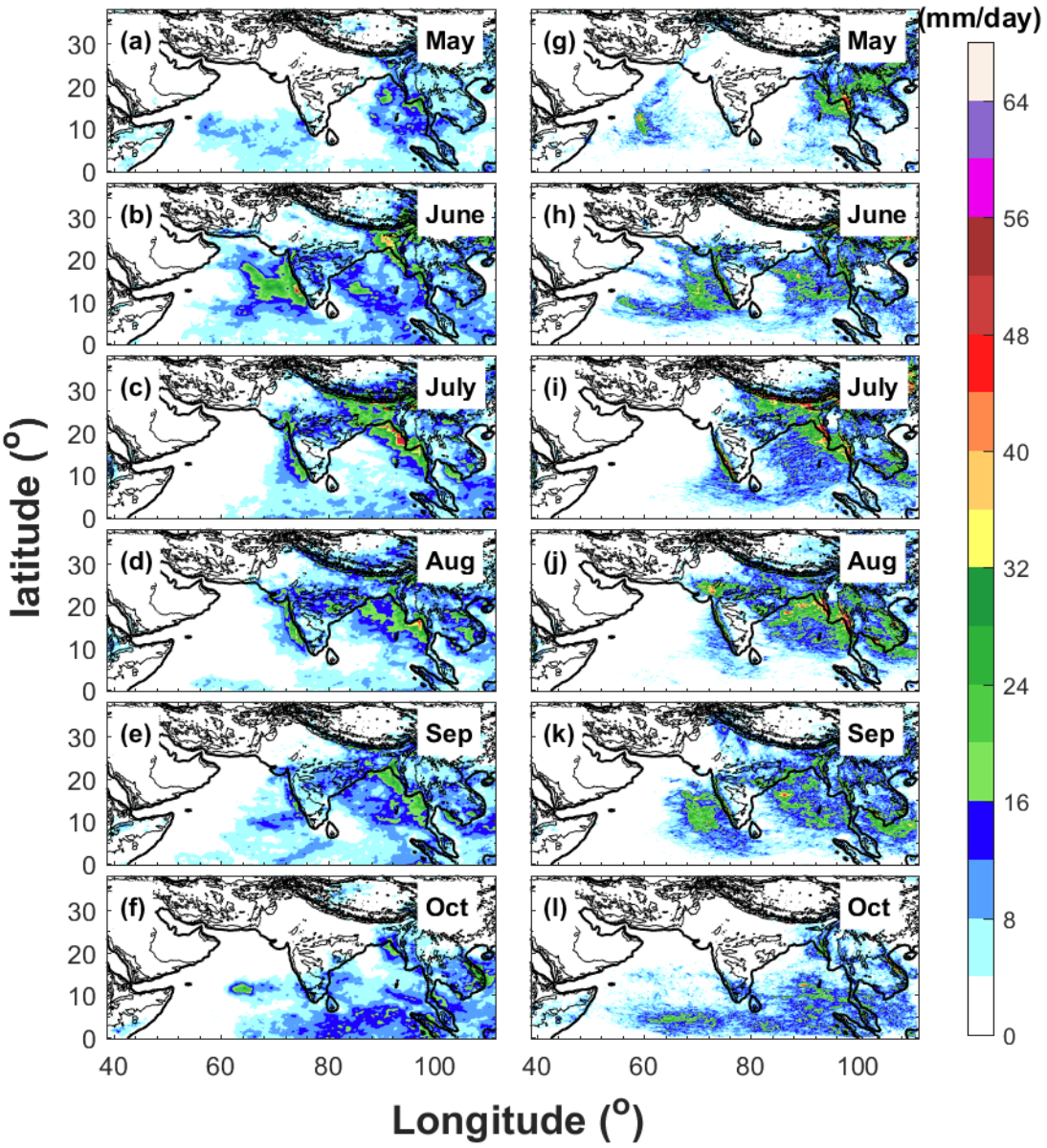

809
810 Figure 6. Spatial distributions of averaged daily surface precipitation from May to October in year 2007
811 derived from (a-f) TRMM and (g-l) WRF-gray.
812

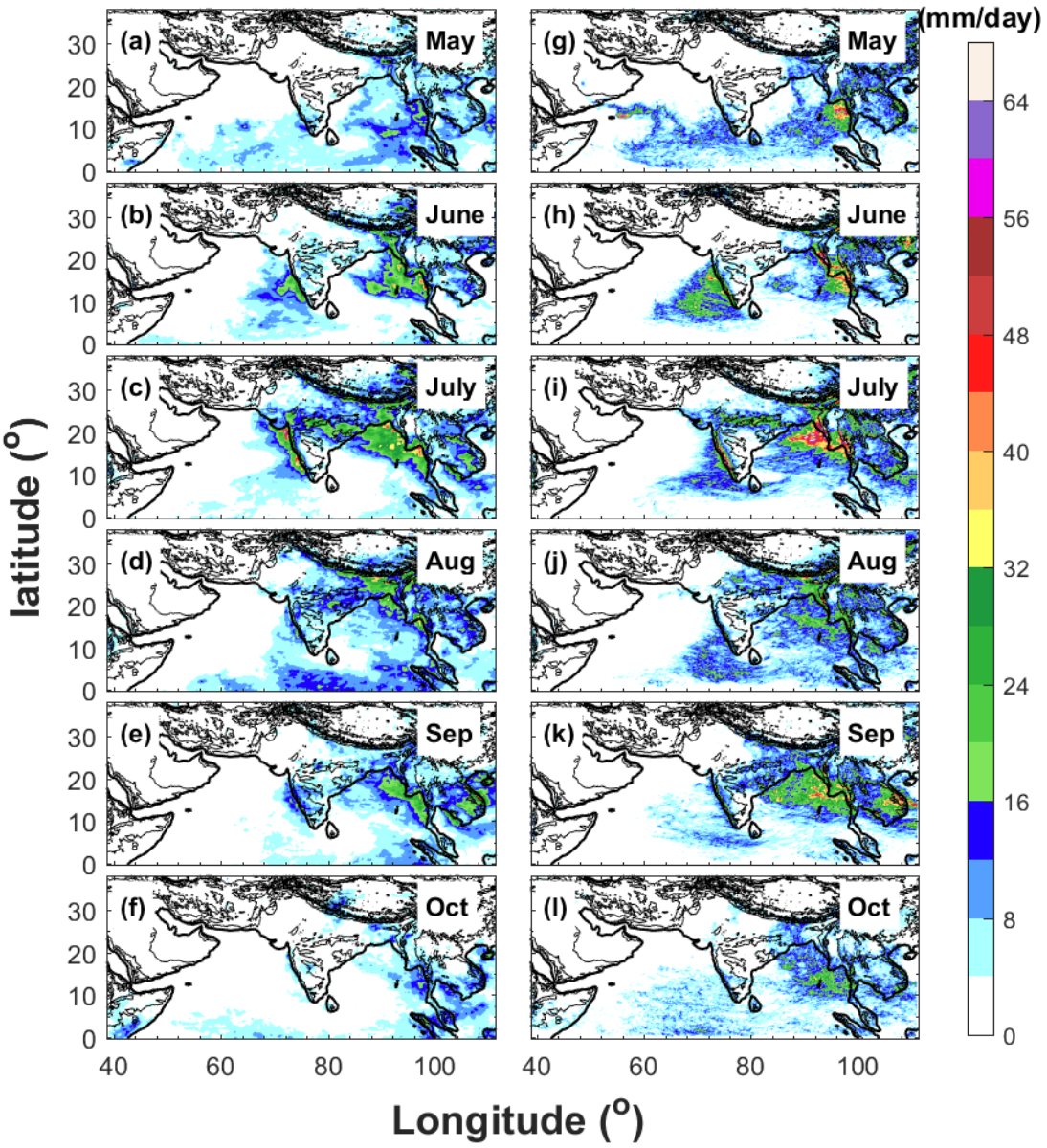

Figure 7. Spatial distributions of averaged daily surface precipitation from May to October in year 2009 derived from (a-f) TRMM and (g-l) WRF-gray.

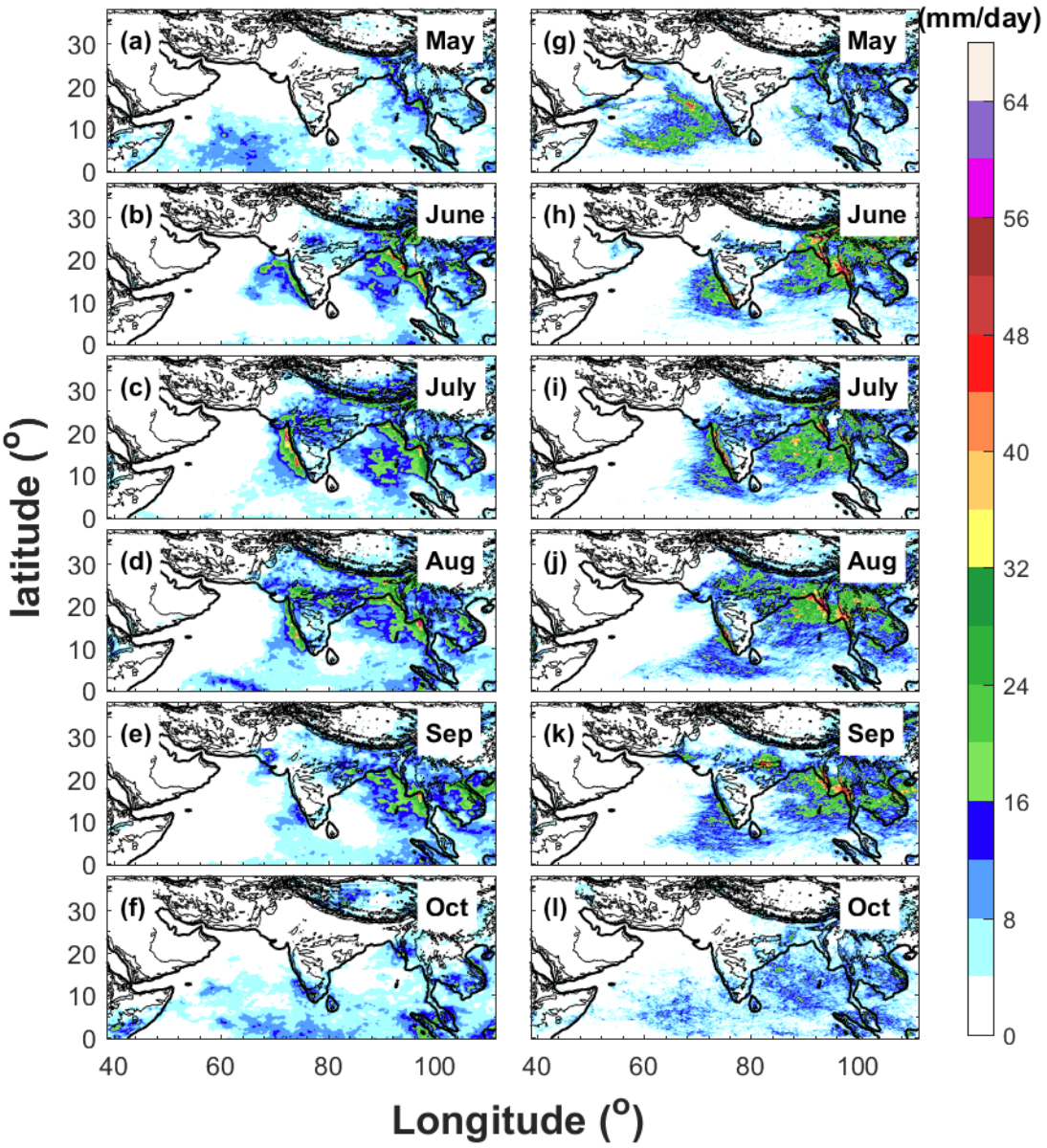

817
818 Figure 8. Spatial distributions of averaged daily surface precipitation from May to October in year 2011
819 derived from (a-f) TRMM and (g-l) WRF-gray.
820

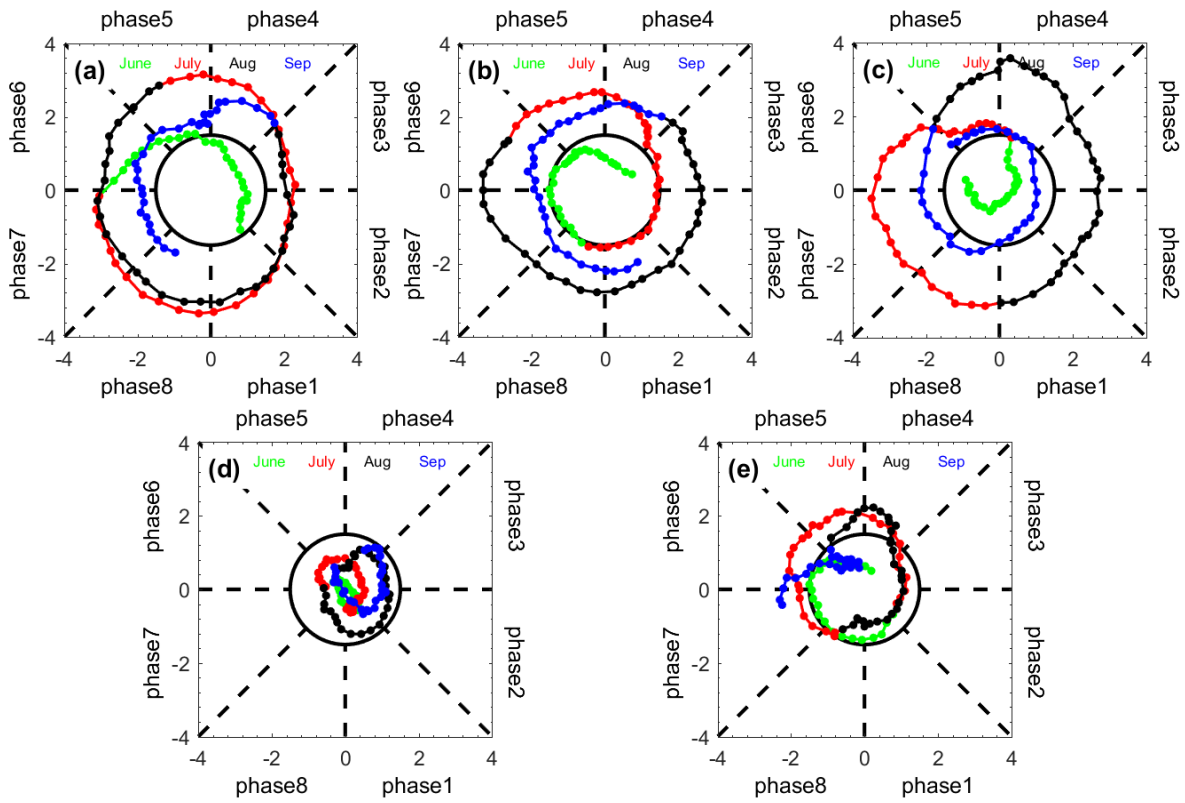

Figure 9. 2D phase space diagrams for the NLSA MISO indices in years: (a) 2007, (b) 2008, (c) 2009, (d) 2010 and (e) 2011. An anticlockwise propagation from the phase 1 represents MISO's northward propagation. The circle centered at the origin has radius equal to 1.5, which is the threshold for identification of significant MISO events.

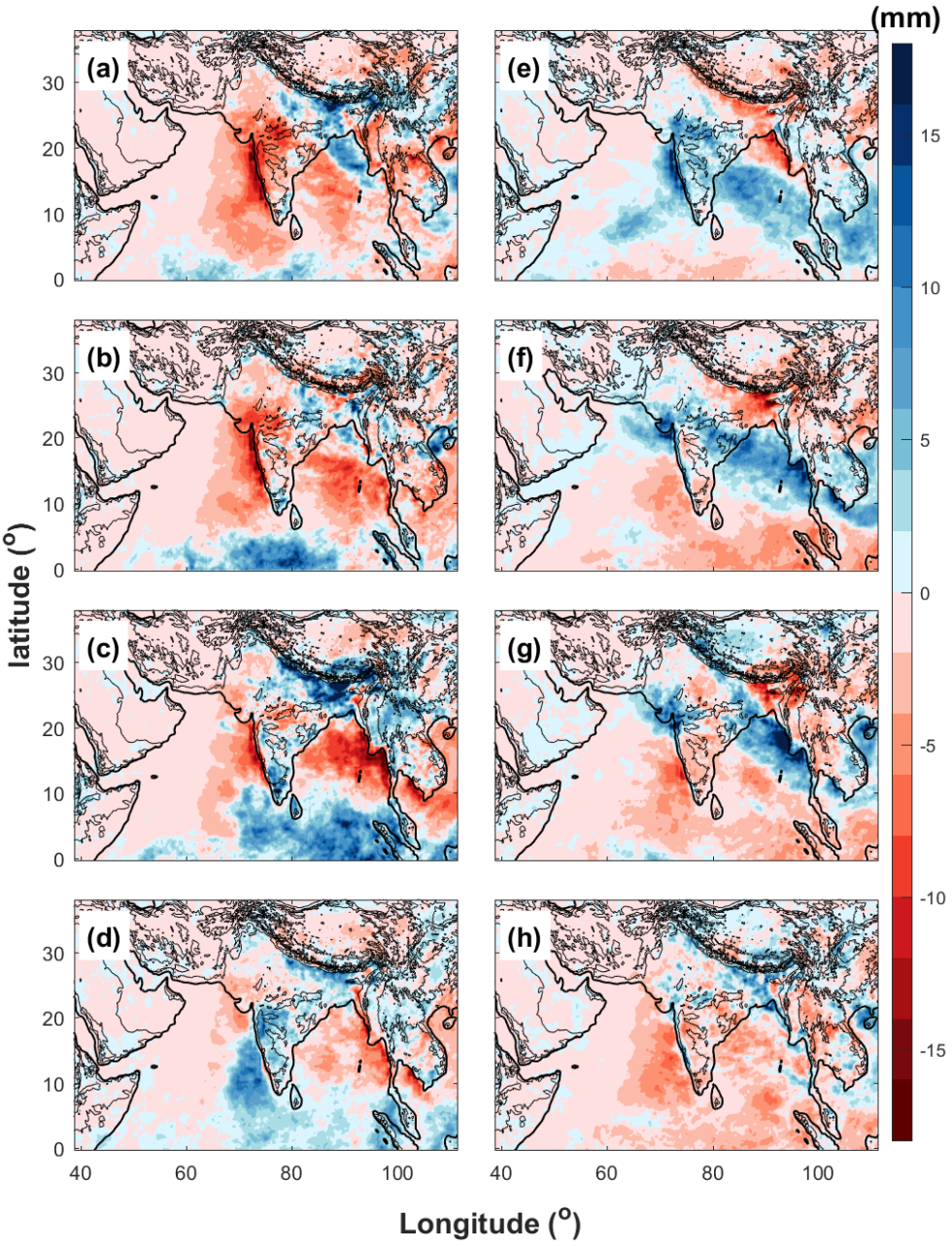

827
828 Figure 10. Phase composites of daily surface rainfall anomalies obtained from TRMM (Figure a-h: phase 1 to
829 8).
830

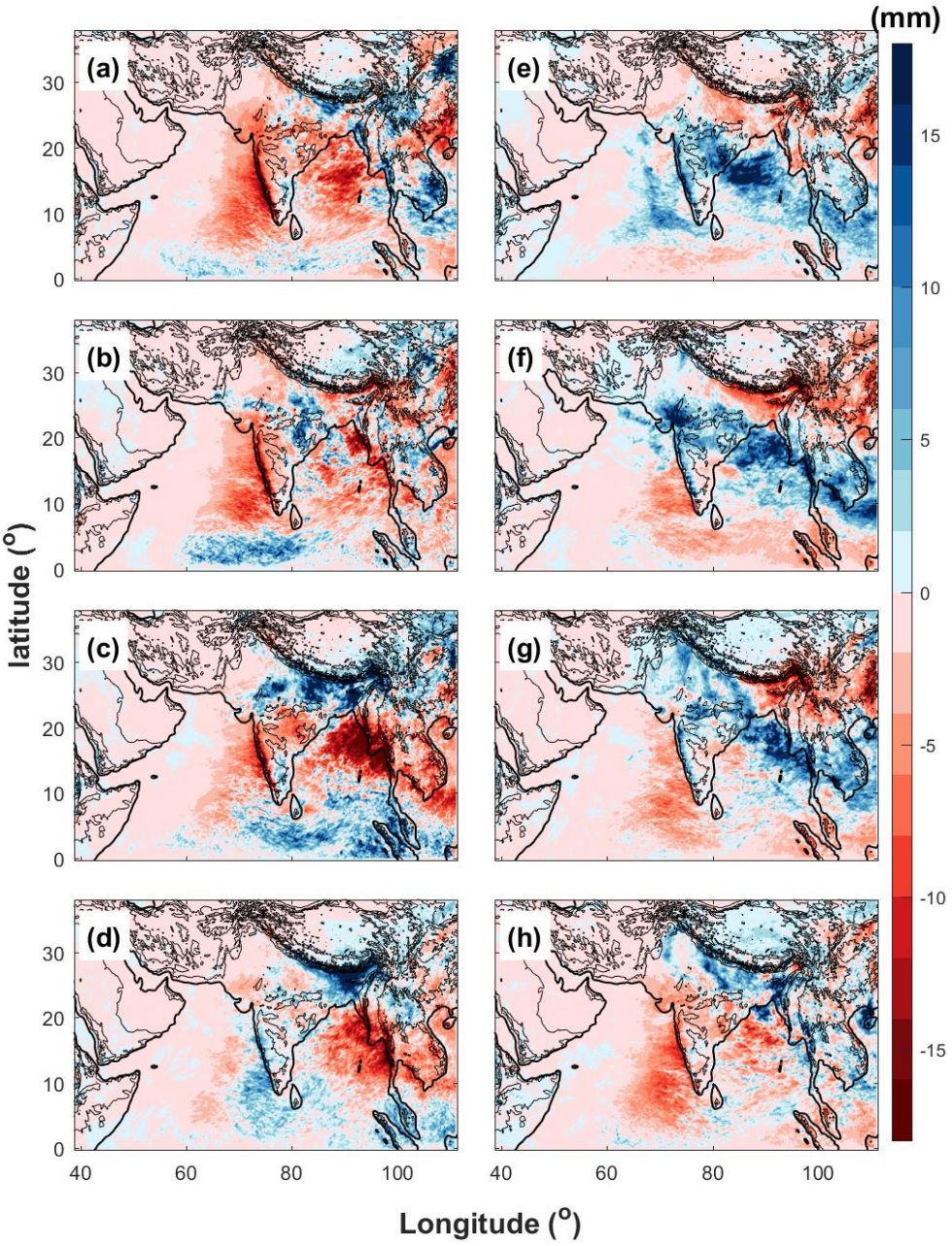

Figure 11. Phase composites of daily surface rainfall anomalies obtained from WRF-gray (Figure a-h: phase 1 to 8).

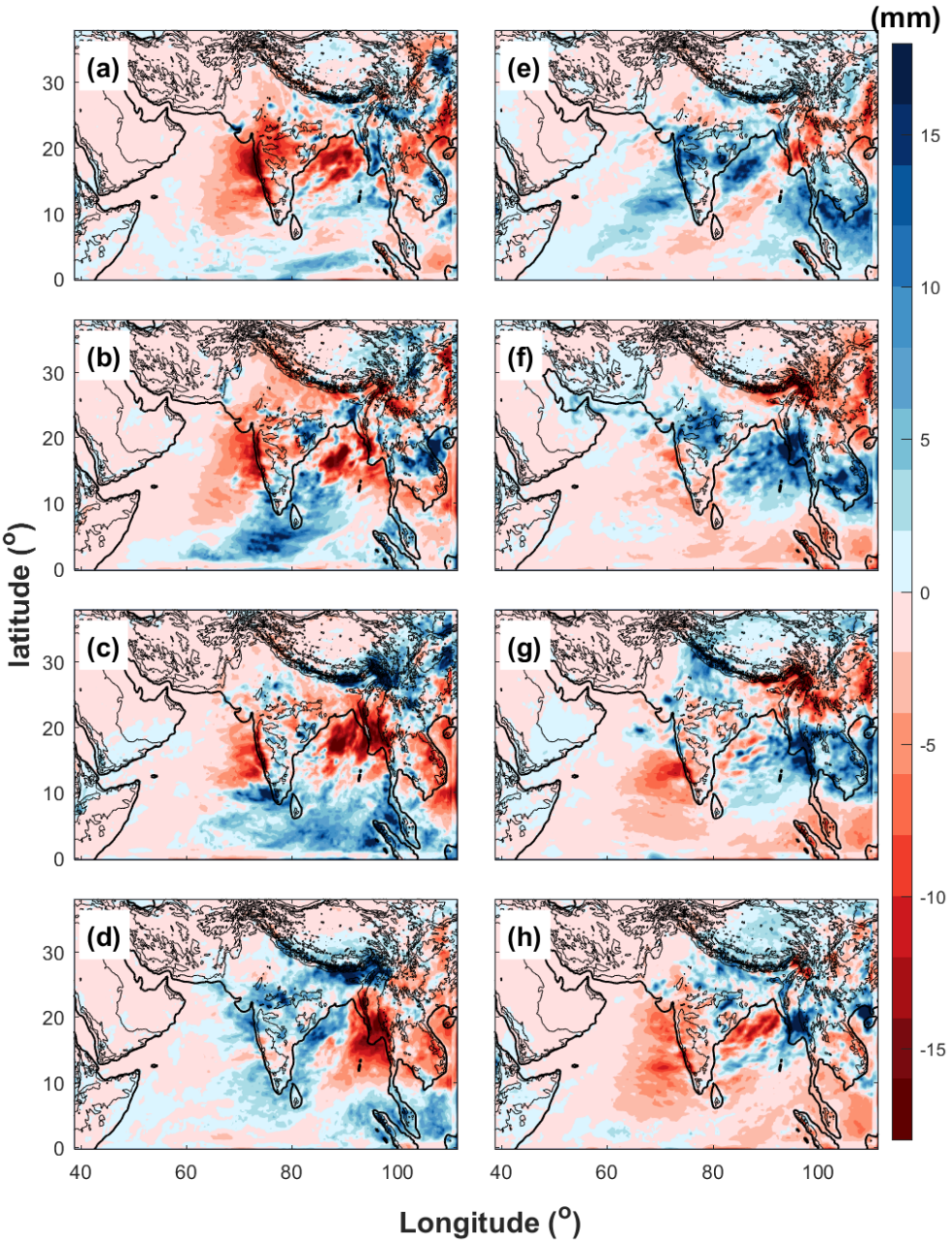

835
836 Figure 12. Phase composites of daily surface rainfall anomalies obtained from WRF-27km (Figure a-h: phase 1
837 to 8).
838

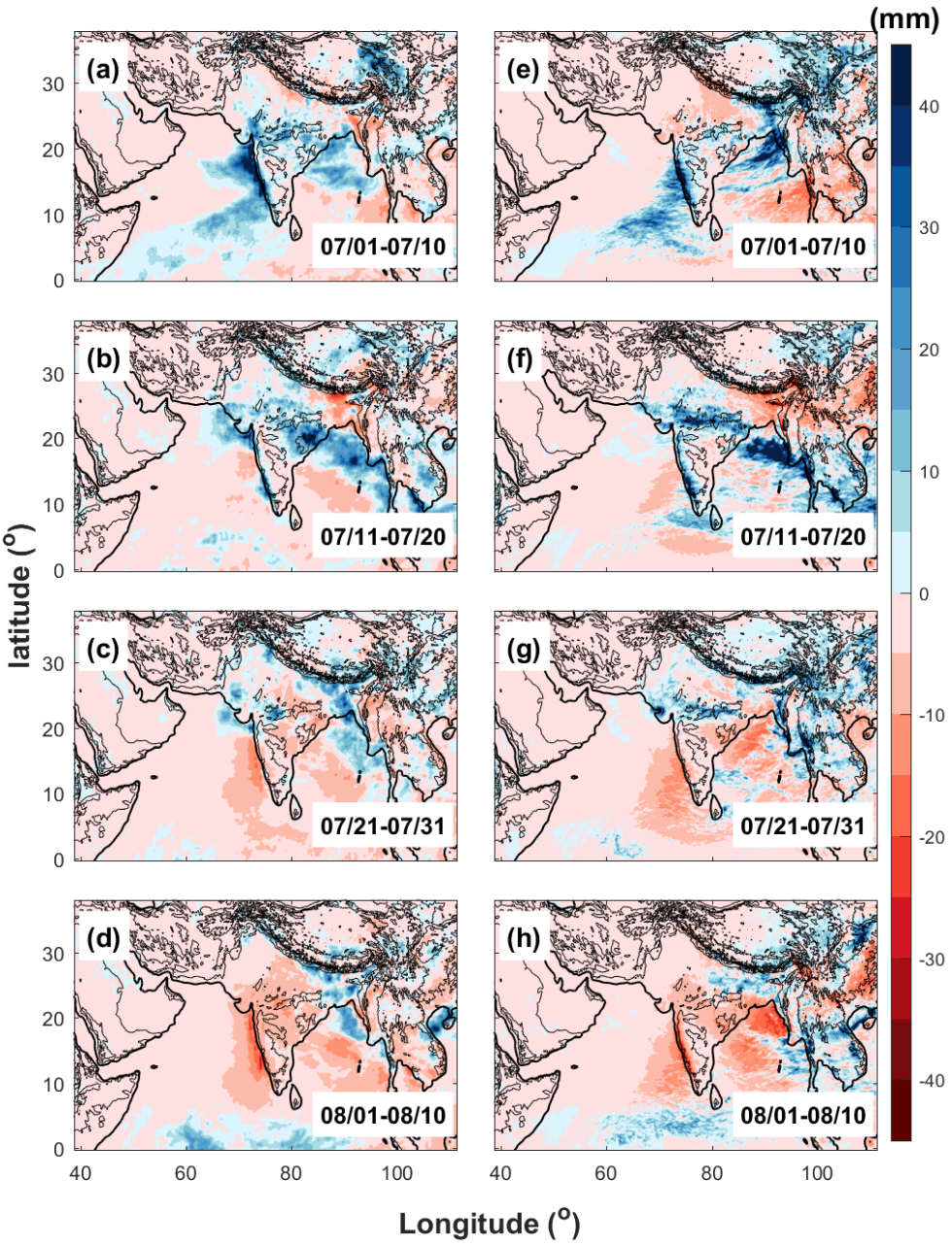

839
840 Figure 13. Spatial distributions of 10-day averaged daily surface rainfall anomalies in (a, e) 1-10 July, (d, f)
841 11-20 July, (c, g) 21-31 July and (d, h) 01-10 August, 2009 derived from TRMM (left panels) and WRF-gray
842 (right panels).
843

844

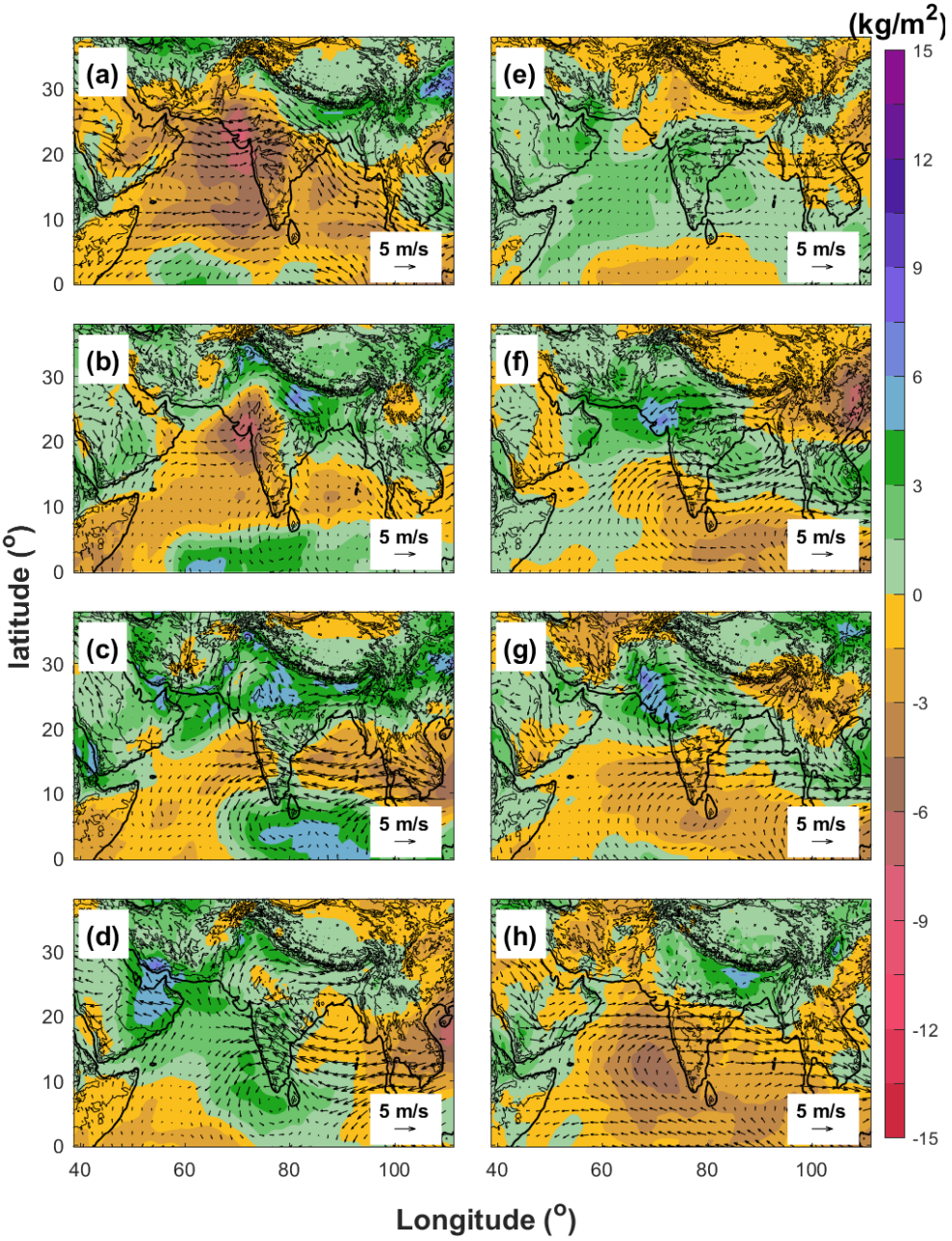

845
846 Figure 14. Phase composites of 850-hPa wind and precipitable water anomalies obtained from ERA-Interim
847 (Figure a-h: phase 1 to 8).
848

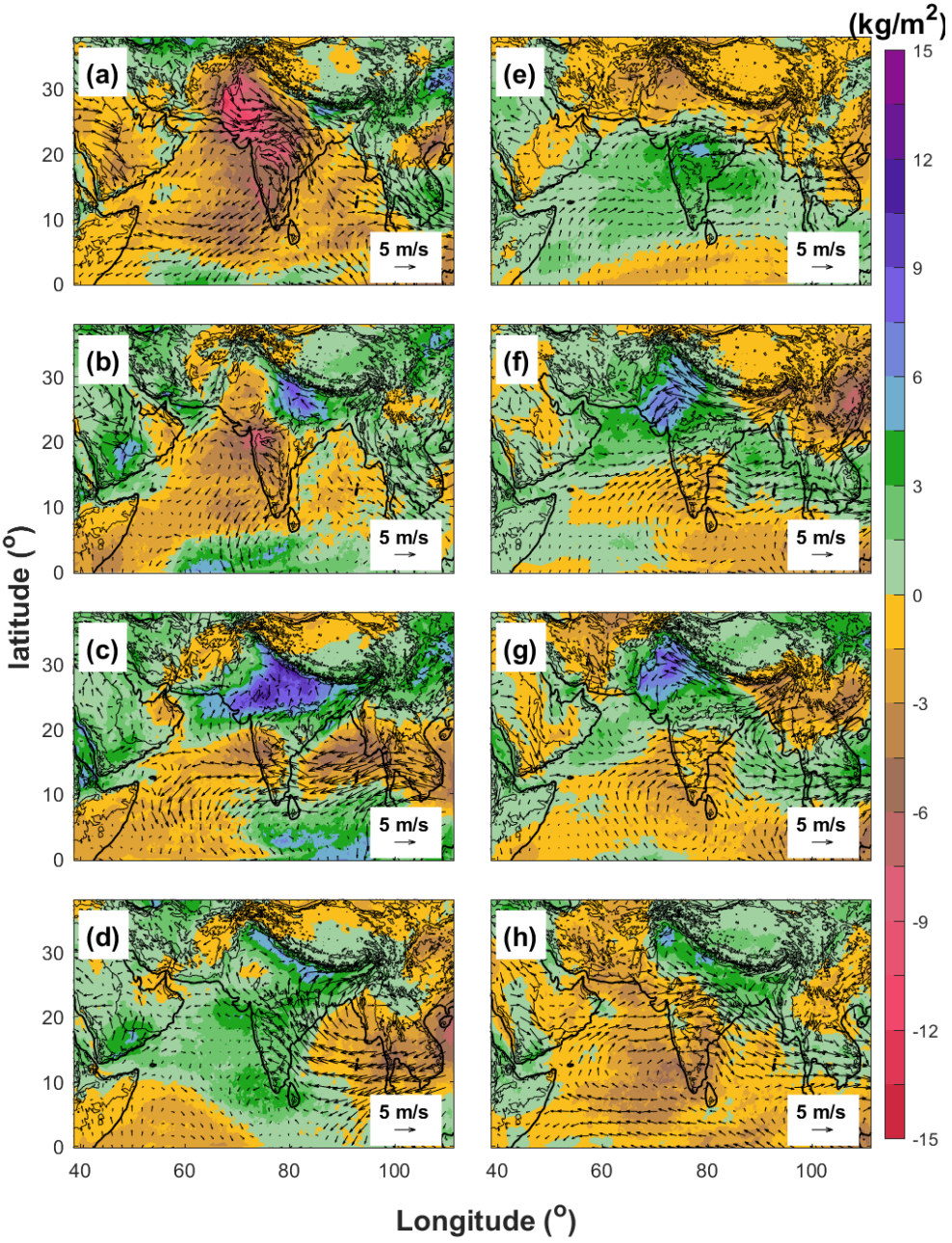

849
850 Figure 15. Phase composites of 850-hPa wind and precipitable water anomalies obtained from WRF-gray
851 (Figure a-h: phase 1 to 8).
852

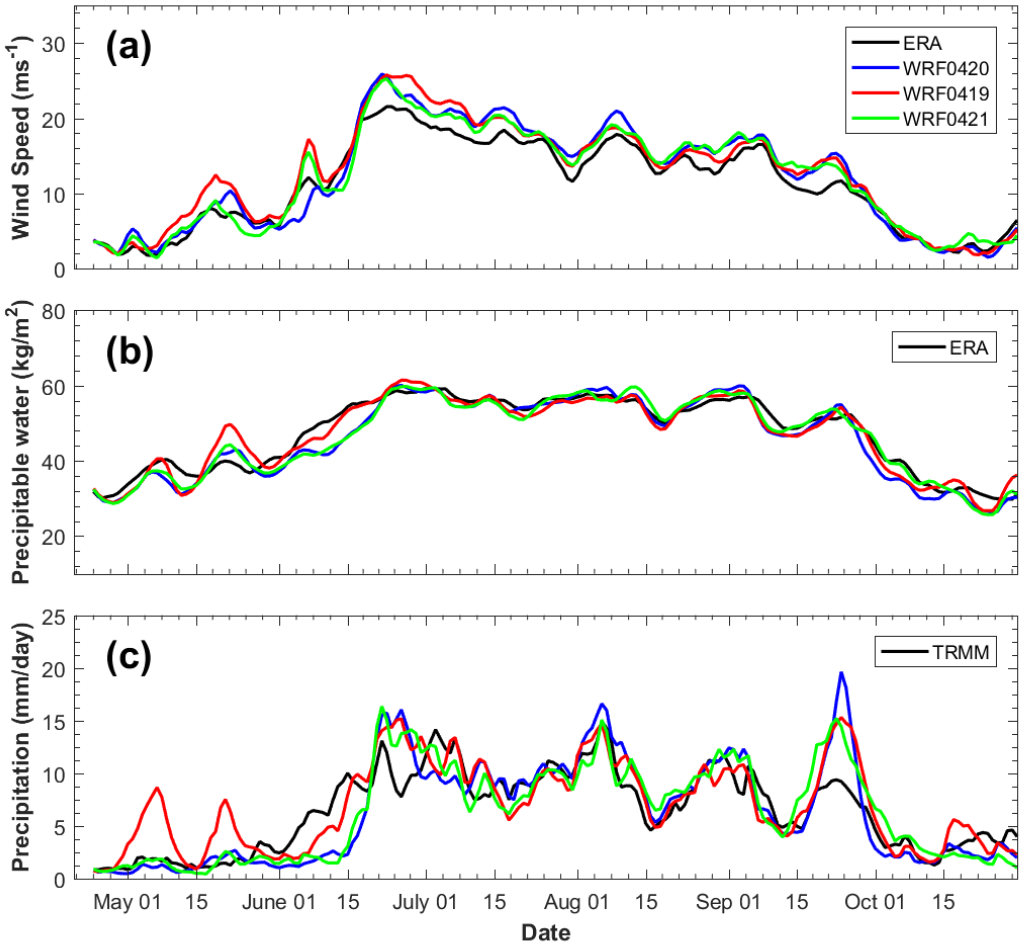

853
854 Figure 16. Temporal evolutions of (a) KELLF indices, (b) precipitable water averaged over the Indian
855 subcontinent and (c) daily surface precipitation averaged over the Indian subcontinent in year 2007 from
856 ERA-Interim/TRMM (black lines), WRF-gray simulation starts from April 20 (blue lines, control run), WRF-gray
857 simulation starts from April 19 (red lines) and WRF-gray simulation starts from April 21 (green lines).
858